Titre: Title:	On the Fabrication of Novel Solid Immersion Lenses for Super-Resolution THz Imaging
Auteur: Author:	Quentin Chapdelaine
Date:	2022
Type:	Mémoire ou thèse / Dissertation or Thesis
Référence: Citation:	Chapdelaine, Q. (2022). On the Fabrication of Novel Solid Immersion Lenses for Super-Resolution THz Imaging [Mémoire de maîtrise, Polytechnique Montréal]. PolyPublie. https://publications.polymtl.ca/10336/

URL de PolyPublie: PolyPublie URL:	https://publications.polymtl.ca/10336/
Directeurs de recherche: Advisors:	Maksim A. Skorobogatiy
Programme: Program:	Génie physique

POLYTECHNIQUE MONTRÉAL

affiliée à l'Université de Montréal

On the Fabrication of Novel Solid Immersion Lenses for Super-Resolution THz Imaging

QUENTIN CHAPDELAINE

Département de génie physique

Mémoire présenté en vue de l'obtention du diplôme de *Maîtrise ès sciences appliquées*

Génie physique

Mai 2022

POLYTECHNIQUE MONTRÉAL

affiliée à l'Université de Montréal

Ce mémoire intitulé :

On the Fabrication of Novel Solid Immersion Lenses for Super-Resolution THz Imaging

présenté par **Quentin CHAPDELAINE**

en vue de l'obtention du diplôme de *Maîtrise ès sciences appliquées*

a été dûment accepté par le jury d'examen constitué de :

Denis SELETSKIY, président

Maksim SKOROBOGATIY, membre et directeur de recherche

Gregory PATIENCE, membre

DEDICATION

I dedicate this thesis to my father and to my mother, who taught me what is dedication, perseverance, and the enjoyment of the work done

Je dédie ce mémoire à mon père et ma mère, pour m'avoir appris ce qu'est la dédication, la persévérance et le plaisir du travail accompli

ACKNOWLEDGEMENTS

I would like to give my warmest thanks to my supervisor, Professor Maksim Skorobogatiy, for his invaluable assistance and insights leading to the writing of this thesis. Your passion for this field is inspiring and your guidance throughout my research makes me extremely grateful to have been a part of it.

A great thanks to my colleagues Kathirvel Nallappan, Ph.D., Hichem Guerboukha, Ph.D., Yang Cao, Ph.D., Raphaël Henry, M.Sc.A., Mathieu Poulin, M.Sc.A., and Guofu Xu, Ph.D. candidate, for sharing your knowledge and giving me your valuable suggestions, ever encouraging and motivating guidance throughout this project.

Un immense merci à Jean-Paul Lévesque, Matthieu Gauthier, Mikaël Leduc et Yves Leblanc pour votre aide tout au long de ce projet.

Et par-dessus tout, merci à ma famille pour leur support constant depuis toujours.

RÉSUMÉ

Dans ce mémoire, j'explore la fabrication de nouvelles lentilles à immersion solide (SIL) à partir de mélanges de poudre de dioxyde de titane (TiO_2) et de polypropylène (PP). Deux stratégies différentes de fabrication de lentilles sont explorées et utilisées pour étudier comment l'augmentation de la concentration de TiO_2 permet d'améliorer la résolution d'imagerie du système. La première stratégie de fabrication de lentilles consiste à presser la poudre de TiO_2 avec une poudre de polypropylène (PP) à la température Vicat du PP tout en contrôlant la concentration de TiO_2 et la porosité de la lentille résultante. La seconde consiste à presser la poudre de TiO_2 dans un hémisphère creux imprimé en 3D avec un filament de PP. Les lentilles sont ensuite caractérisées physiquement et optiquement, et leurs indices de réfraction sont comparés aux estimations théoriques utilisant le modèle de Bruggeman des milieux effectifs. Les mesures expérimentales dans la gamme de fréquences THz montrent que la limite de résolution de la lentille SI diminue en effet de manière inversement proportionnelle à son indice de réfraction. De plus, je démontre que plusieurs lentilles battent la limite de diffraction d'Abbe de $\lambda/2NA$ et atteignent une résolution aussi basse que $\sim 0.2\lambda$, ce qui est comparable aux meilleures résolutions rapportées dans la littérature lors de l'utilisation de lentilles à immersion solide en Silicium plus standard et très dispendieuses. La technique de fabrication simple et efficace en termes de coût pour la fabrication de lentilles SIL rapportée dans ce mémoire a un fort potentiel pour la fabrication de composants d'imagerie THz et promet une amélioration des performances des SIL au-delà des solutions en Silicium les plus courantes.

ABSTRACT

In this thesis, I explore the fabrication of novel Solid Immersion lenses (SIL) from the powder mixes of titanium dioxide (TiO_2) and Polypropylene (PP). Two different lens fabrication strategies are explored and used to study how the increase in the concentration of TiO_2 enables the improvement of the system imaging resolution. The first lens fabrication strategy uses pressing the TiO_2 powder with a polypropylene (PP) powder at the Vicat temperature of PP while controlling the concentration of TiO_2 and the resultant lens porosity. The second design consists in pressing the TiO_2 powder in a hollow hemisphere printed in 3D with a PP filament. Lenses are then characterized physically and optically, and their refractive indices are compared to the theoretical estimates using the Bruggeman model of effective media. Experimental measurements in the THz frequency range show that the SI lens resolution limit indeed reduces inversely proportional to its refractive index. Moreover, I demonstrate that several lenses beat Abbe's diffraction limit of $\lambda/2NA$ and reach the resolution of as low as ~0.2λ, which is comparable to the best resolutions reported in the literature when using more standard and very expensive silicon solid immersion lenses. The cost-efficient and simple fabrication technique for SI lens fabrication reported in my thesis hold strong potential for THz imaging component fabrication and promises performance enhancement of SI optics beyond the leading silicon solutions.

TABLE OF CONTENTS

LIST OF TABLES

LIST OF FIGURES

LIST OF SYMBOLS AND ABBREVIATIONS

λ	Wavelength
AFM	Atomic Force Microscope
BWO	Backward-Wave Oscillators
CW	Continuous Wave
EM	Electromagnetic
FFF	Fused Filament Fabrication
FDM	Fused Deposition Modeling
FLM	Fused Layer Modeling
FWHM	Full Width Half Max
HDPE	High Density Polyethylene
IR	Infrared
NA	Numerical Aperture
NDA	Negative Differential Resistance
NF	Near-Field
OPA	Optical Parametric Amplifier
PCA	Photoconductive Antenna
PP	Polypropylene
PTFE	Teflon
QCL	Quantum Cascade Lasers
RI	Refractive Index
ROI	Region Of Interest
RTD	Resonant Tunneling Diode
SEM	Scanning Electron Microscope
SIL	Solid Immersion Lens
SNOM	Scanning Near-field Optical Microscope
s-SNOM	Scattering-type Scanning Near-field Optical Microscope
SNR	Signal-to-Noise Ratio
SWS	Slow Wave Structure
THz	Terahertz
THz-TDS	THz Time-Domain-Spectroscopy
TiO_2	Titanium Dioxide
TWT	Travelling-Wave Tubes

CHAPTER 1 INTRODUCTION

The terahertz (THz) frequencies, or the THz gap, as it is often referred to in the literature, are a portion of the electromagnetic (EM) spectrum between the end of the infrared (IR) and the start of the millimeter waves. From a modern perspective, it is a range where the latest advances in imaging techniques and telecommunication meet. The THz gap is commonly described as being between 0.1 and 10 THz, or 3 mm to 30 μm. This range is known as a gap because of the lack of scientific interest in these frequencies for the better part of the last two centuries, when technology was not advanced enough for either the generation or the detection of these frequencies. The high absorbance in water of these waves combined with the low power achievable makes their transmission very difficult and their applications few and far between. The advances in laser science and telecommunications that have occurred since the 1980s have forced a reconsideration of this consensus. The femtosecond lasers, non-linear optics, and microfabrication methods opened the door to new generations of antennas, sources, and detectors of THz. The new accessibility to the THz gap fostered the interest in this forgotten spectrum, which is now the new frontier to many modern technologies.

In the telecommunication field, 5G technology already pushes the bandwidth to the dozens of GHz. THz will then become the next step to take in order to improve wireless communication around the world. In the electronic field, the THz waveguides could eventually be more suited for the increased speed in commutation of classic electronic signal processors [1]. In the new materials field, THz can modulate the properties of semiconductors, giving them a tunability that will prove useful in the future [2].

The imaging industry is one of the fields that are the most interested in the development of THz. The THz radiation could be a solution for problems met by many applications. The fact that they do not interact with most non-polar dielectric materials (such as papers and fabrics), that their frequency corresponds to the low energy levels of the hydrogen bond [3], and that they can be easily used to find the dielectric function of semiconductor wafers [4], allows them to offer unique information in many spectroscopic and imaging applications. The longer and non-ionizing wavelengths of the THz are also less damageable for humans, and could therefore be useful for *in vivo* imaging in biomedical applications [5]. Longer wavelengths also facilitate the fabrication of

THz waveguides, whose polishing becomes less restrictive, and where minor defects become less diffractive. Many polymers also proved to be very good materials for THz guiding, making their fabrication less costly than in the visible region.

THz are still a new science, and many challenges remain to be solved before seeing more concrete implementation in industry. One such challenge in the field of imaging is due to the diffraction limit in the resolution of microscopes, which significantly affects the potential of simple confocal THz microscopy.

Challenges and objectives of solid immersion imaging

Resolution can be defined by the capacity to distinguish two different and adjacent spots on an image. Therefore, an imaging system that relies on the focus of a laser beam on a sample to create a pixel is limited by the radius, or spot size, of the beam. It must then be stressed that no matter how sophisticated it is, a beam of EM waves focused through a lens system cannot have its size reduced by an arbitrarily high factor. As an example, we can consider the gaussian beam, which is the best representation of any laser beam; its most focused position will be described by its *waist*. When focused by a thin lens system, the waist of the beam will be found in the focal plane of the lens and can be expressed by

$$w = \frac{\lambda}{2\,NA} = \frac{\lambda}{2 * n * \sin(\theta)} \qquad (1-1)$$

where λ is the vacuum wavelength of the beam, $A = n\sin(\theta)$ is the numerical aperture of the lens focusing the beam, θ is the half-angle of the cone produced by the focused light and n is the refractive index (RI) of the medium in which the beam propagates. This expression is called Abbe's diffraction limit, named after Ernst Abbe, the German physicist who set the standards for the fabrication of microscopes in the second half of the 19th century.

From Equation 1-1, we can see that the imaging wavelength used in a system is a limit for the final resolution of the system. A microscope lens in free space with a numerical aperture of 0.6 would therefore have a resolution of around 0.8 λ. Such a system in the visible wavelengths could not resolve details below a few hundred nanometers. Although for many applications, such a resolution

would not be an issue, the new technologies rely more and more on nanofabrication techniques, and nanoscopic precision in imaging systems gathers interest from multiple industries. Moreover, when talking about THz imaging, λ ranges from 30 μm to3 mm, and a resolution close to λ is extremely binding. To enable the full potential of THz imaging, this problem needs to be addressed.

This issue with diffraction in imaging was previously studied by many scientists working with different parts of the EM spectrum. From their work arose a vast literature on what is known as super-resolution, i.e., the system for which the resolution is not limited by the diffraction limit. Those systems use different physical concepts to avoid the diffraction problem, such as fluorescence markers or probes and apertures in the near-field (NF) of the sample. One of those techniques, solid immersion imaging [6], has already been applied to THz waves. Resolution down to 0.15 λ have been reported, which is clearly better than Abbe's limit [7]. The resolution of the solid immersion imaging depends on its solid immersion lens (SIL), a hemispherical lens whose RI needs to be as high as possible to reduce the diffraction limit. In the THz field, the optimization of those lenses is still a new topic, and the fabrication of these lenses is not perfectly standardized yet.

Structure of the thesis

This thesis will address the design, fabrication, and characterization of solid immersion lenses. It will be divided into four chapters. Chapter 1 presents the literature review and the theoretical background explaining the utility and challenges of THz imaging, and the need for resolution in its applications. It also gives references to the literature in order to better appreciate the results obtained. Chapter 2 presents the methodology of the experiments; the choices faced in the design of the SILs and the fabrication of solid immersion microscopes are addressed and detailed. In Chapter 3, an article submitted to the journal Optics Materials Express and titled "*Fabrication and Characterization of High Refractive Index Solid Immersion Lens for Super-resolution Terahertz Imaging*" is presented. In this article, we present the details of the fabrication of four SILs based on two designs which are intended to maximize the resolution of a solid immersion system with inexpensive lenses built with titanium dioxide powders A shorter version of the article was published for the conference 2022 IEEE Summer Topicals Meeting Series. Finally, in Chapter 4,

we discuss the results obtained. The initial assumptions of this project are tested, and potential improvements are presented for future research.

CHAPTER 2 LITERATURE REVIEW

This chapter gives an overview of the scientific background of this project. First, it sets the historical context of light diffraction in microscope systems and the advancements that yielded the formulation of the minimal spot size of a beam focused through a lens. Then, it moves toward the THz, their generation for imaging purposes, and the resolution needed for some specific applications. The historical solutions to the diffraction limit are then presented, among which the solid immersion imaging system. Finally, the subject of building high RI optical components for THz is addressed as we present potential fabrication techniques for SILs that have been tested, as well as the results they have yielded.

2.1. The diffraction limit in imaging

2.1.1. Historical context

The first extensive theorization of microscopes as an optical system was made by Ernst Abbe in the late 1860s, as advances in science and technology made the fabrication of high-quality lenses possible, both in the visible and in the near IR region [8]. While very powerful telescopes had existed for centuries, microscopy posed very specific challenges. The first was due to off-axis light coming from the sample and causing aberrations. The second was because of the need to use the same lens to illuminate the sample and collect the reflected light, which increased the potential flaws in the optics used. These concerns made the first microscopes very limited in terms of their resolution. At the time, the explanation for this limitation was errors due to experimental conditions. However, Abbe saw it as a physical limit caused by light's nature as a wave and the existence of diffraction within a focused beam. He proved his point by fabricating the best lenses available at the time and showing experimentally what is known today as the diffraction limit. As shown in Figure 2-1, this limit is produced by the interference of multiple light waves coming from the object plane of the focusing lens.

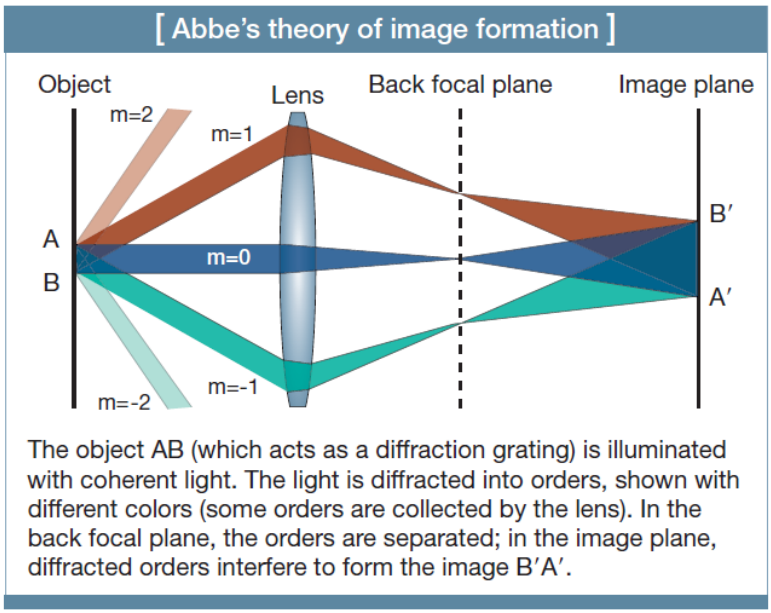

Figure 2-1: Schematic of Abbe's theory of image formation, and his physical diffraction limit. Reproduced from [8]

Abbe concluded that the best solution to push back this limit was to increase the ratio of lens width over the focal lens. Increasing the angle of the cone produced by the focused beam would allow a higher and more precise constructive interference on the central peak in the image plane. Abbe would formulate the term numerical aperture (NA) to quantify this resolution power. The numerical aperture is defined as

$$NA = n\sin(\theta) \qquad (2-1)$$

where n is the RI of the environment of the image plane and θ is the one-half angle made by the cone of focused light rays between the lens and the image plane. Maximizing the numerical aperture would maximize the resolution. The use of RI within the NA expression was a path to improve the resolution already traced by Abbe, and which we will discuss further in Section 1.3.

As the context evolved since Abbe's work at the end of the 19th century, image formation theory refined itself to a much higher level. As the authors were trying, on one side, to break the limit of nanoscopy [9], and on the other to push back the resolution for longer wavelengths [7], the mathematical formulation of this limit became much more precise. Indeed, theoretical development using the Fourier analysis also yielded similar results, and can be found in most manuals relating

to optics and photonics such as [10] and [11]. These results, which for decades challenged the progress in the resolution of microscope systems, attracted the attention of the scientific community. In the following years, and in the context of quantum mechanics development, Heisenberg came up with the uncertainty principle, which also used the wave-particle behaviour of light to impose a limit to the information that can be measured empirically. The two limitations meet in a limit case of resolution, one in which a light beam would be focused in a pupil smaller than half its wavelength. In this situation, the diffraction perceived on a screen at some distance from the pupil would be bigger than the pupil, and the diffraction limit would still be respected (except in the near-field, which we will see in Section 1.3.2) [12].

In 1952, Toraldo di Francia extensively studied the phenomenon of diffraction and proposed that a non-uniform pupil (or a pupil filter) could force diffraction to focus its central maximum in a smaller spot size than the diffraction limit [13,14]. It appears, however, that the side lobes produced by the interference pattern in the far-field would pose other problems limiting the resolution [15]. Toraldo di Francia also popularized the term “super-resolution” to describe a resolution that would beat the diffraction limit. To this day, this limit is still considered as one of the main physical limitations encountered in optics. Although different solutions were invented to avoid it, most require expensive and complicated instruments, and often need to sacrifice other parameters to improve the spatial resolution (see Section 1.3).

2.1.2. Measuring the size of a beam

When dealing with a laser beam, it is useful to express its shape as a gaussian function. Indeed, this function, expressed in the form

$$U(z) = A_0 \frac{W_0}{W(z)} \exp\left[-\frac{\rho^2}{W^2(z)}\right] \exp\left[-jkz - jk\frac{\rho^2}{2R(z)} + j\varsigma(z)\right] \qquad (2-2)$$

can be derived from the Fresnel approximation of paraxial beam and is a solution to the Helmholtz differential equation describing every EM wave. A full derivation of this expression from the Maxwell equations can be found in reference [10], section 3.1. Although not every electromagnetic radiation produced by a laser or an antenna precisely follows Equation 2-2, it is convenient to

assume that the beam resembles it to some degree [16]. This is because the gaussian beam describes a beam whose envelope width shows a variation in the propagation axis z along the shape

$$W(z) = W_0 \sqrt{1 + \left(\frac{z}{z_0}\right)^2} \qquad (2-3)$$

which can be very reasonably generalized to most guided beams of light. At its minimum ($z = 0$), the diameter of the beam is called the *waist* and is given by

$$W_0 = \sqrt{\frac{\lambda z_0}{\pi}} \qquad (2-4)$$

where z_0 is the Rayleigh range, i.e., the distance from the waist where the beam width is twice the waist. Once again, Equation 2-4 shows that this smallest radius achievable with a laser beam is wavelength-dependent.

Measuring the waist of a beam is crucial in characterizing it, and one of the most popular methods for doing so is the knife-edge experiment. This technique consists of moving a razor blade in the plane orthogonal to the propagation of the beam (see Figure 4-10). As the blade slowly moves in the plane, a detector records the profile of light intensity either on the other side (transmission mode) or the reflected light intensity (reflection mode). In reflection mode, the power will change from zero to its maximum as a function of the position of the edge of the knife. Afterwards, one can fit a gaussian shape on the data acquired to reproduce the shape of the beam and its width [17,18]. In the case of an imaging system, the slope of the beam profile can be used to extract the resolution of the system. Measuring the derivative of the intensity yields another gaussian function whose FWHM gives the region over which the slope is the highest, and henceforth the distance over which the knife-edge appears in the beam. The FWHM of the derivative is a commonly used measure of the resolution of an imaging system in the literature [7].

2.2. Imaging with THz waves

In this section, we explore the challenge of imaging in THz. Some of the most practical THz sources used in the literature for imaging purposes (meaning sources compact enough to hold on an optical table while providing enough power and a directional enough beam to be used in imaging) are listed and explained. A few applications of THz imaging in the literature are proposed to give an idea of the magnitude of resolution needed, and the field where it would be used.

One of the main reasons for the description of THz as a “gap” is because of the rarity of reliable and powerful sources to emit these radiations [1]. As we can see in Figure 2-2, research in the field exploded at the beginning of the 1990s, essentially because those sources became available. Then followed the interest in imaging, as those sources became cheaper and more stable. As the topics presented in this thesis can be applied to both imaging and spectroscopy, this section covers continuous wave (CW) and pulsed sources, as both have their advantages for specific applications. Although CW sources have more resolution frequency-wise [19], pulsed imaging allows quicker results thanks to the treatment of all frequencies at once and they often have more power too. In the case of coherent wave imaging, also called synchronous detection, sensors for THz with phase information typically have similar working principles, although reversed, as the THz sources. This section will therefore focus on the generation of THz for imaging purposes. More complete reviews can be found in the literature for specific kinds of sources, such as those using a surface phenomenon [20], those whose size holds on a table top [21], or those whose purpose is for imaging [22]. The objective of this section is to highlight the variety of sources possible for THz radiation. A proper understanding of these sources helps to appreciate the limitation of THz super-resolution techniques presented in the next section.

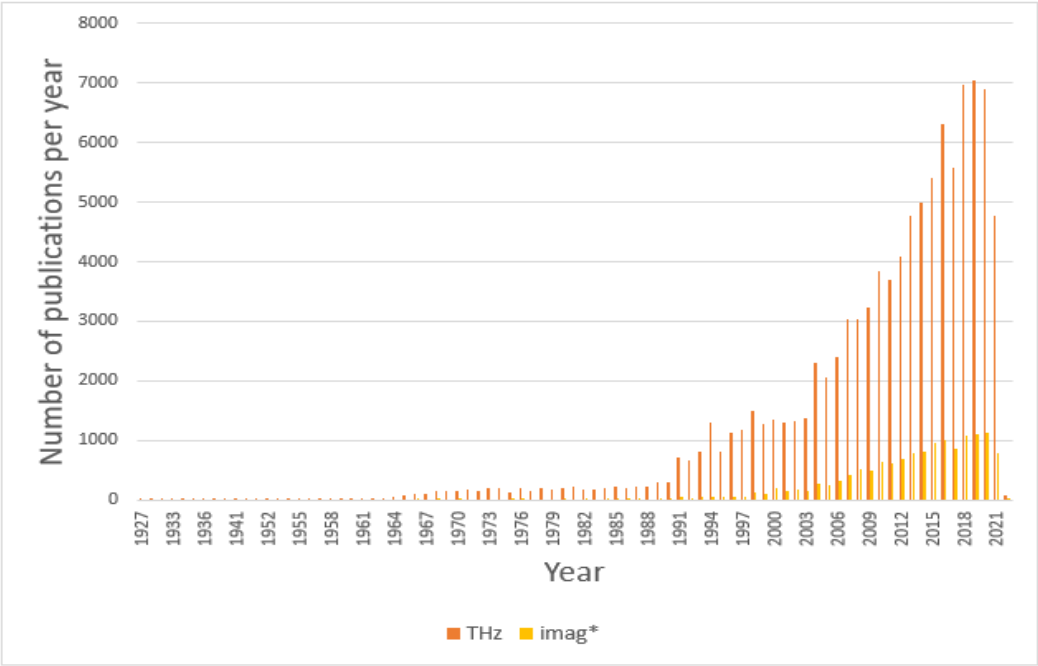

Figure 2-2: Evolution over the years of the new number of publications recorded on Web of Science whose titles include the terms “THz” OR “Terahertz” OR “far infrared” OR “submillimeter wave*” OR “submillimetre wave”. Data is compared to the articles whose title also contained “imag*”.

2.2.1. Generation of CW THz

CW THz sources are older than their pulsed counterparts who heavily rely on the ultrafast laser which appeared at the end of the 1980s [1]. They were mostly developed in the context of a telecommunication field depending heavily on antennas and the ability of an electronic system to identify phase and amplitude information from the signal. Considering the difficulty of producing THz with the same technology as the microwaves, a wide variety of setups were explored to generate these radiations, using multiple physical schemes. Their higher spectral resolution makes it interesting for spectroscopy applications in solid-state samples, where linewidths can be a few tens of GHz [19], which is much better than in IR spectroscopy [23].

The research on THz CW sources can be summarized in four categories: Direct THz lasing, frequency-up conversion of microwaves, frequency down-conversion of visible/IR waves, and vacuum electronics.

2.2.1.1. THz lasers

The first category consists in producing THz radiation with the lasing effect. This idea is a natural extension of the study of far IR radiation, which was mainly produced by gas lasers. Therefore, the THz gas lasers typically consist of a CO_2 laser pumping a medium with a vibrational or rotational absorption band in the THz spectrum (e.g., HCOOH, CH_3OH, and CF_2Br) [23]. Those lasers typically offer enough power for practical application, but suffer also significant inconveniences, such as their large sizes and a lack of tunability [24]. This explains their rarity in modern THz setups. These problems are addressed by the development of quantum cascade lasers (QCL) in the last two decades [25]. QCLs additionally allow mode-locking when complemented by a high-quality absorber and the production of very short THz pulses [26]. However, these lasers need to be cooled at extremely low temperatures for CW operation (below 199 K), but can have small output power in pulsed operation at room temperature [27]. These factors make THz lasers a promising technology, though not a practical one for imaging in their actual state.

2.2.1.2. Frequency up conversion and electronic sources

The second category consists in using electronic components such as diodes (source) and transistors (detector) designed to increase the frequency of an electronic signal into the THz range and then amplify it to enable its transmission [23]. In terms of THz generation, specific diodes, such as Gunn diodes, impact ionization transit time diodes, and resonant tunneling diodes (RTD), have been reported as interesting prospects for generating THz radiations. For these devices, THz generation is due to their negative differential resistance (NDA). This phenomenon describes a compound semiconductor whose I-V curve reaches a peak (see Figure 2-3 b), and therefore has a negative slope on a certain region, meaning a negative resistance. Such a compound can be used to amplify a signal and, in a way comparable to a laser, achieve oscillation when a resonance condition is met.

A good example of such a transmitter is a RTD, like the one presented in reference [28]. This source achieves NDR by placing the diode in a quantum well (see Figure 2-3 a). When the amplified energy level of the diode is in resonance with the energy level of the quantum well, the diode emits an oscillated amplified signal that can be tuned in the THz region. This tuning requires

the right energy level in the semiconductors used in the diode (InP-based semiconductors have reportedly been efficient for THz generation [29]), and a quantum well designed in consequence.

This category of sources is very important in the field of THz for their tunability, low cost, programmability of the emitted signal, and the potential to be produced on a wide scale [30]. In terms of imaging, however, these sources rarely produce more than 100 μW of THz radiation at room temperature, and this power decreases significantly after 1 THz [29]. They are currently more used in telecommunication applications.

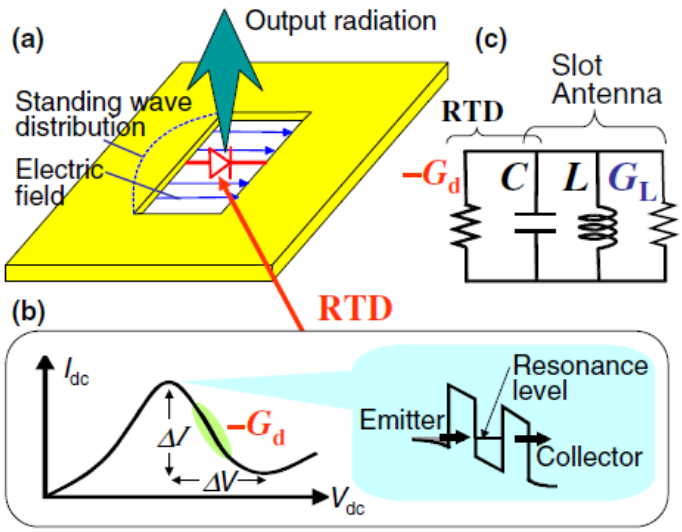

Figure 2-3: a) Schematic of a resonant tunneling diode, b) typical I-V curve expected for the source and c) equivalent circuit. Reproduced from [28]

2.2.1.3. Frequency down-conversion and optical sources

The third category is the most used in imaging. It consists in using a laser signal and converting down its frequency to the THz range, thanks to a photomixer (Section 1.2.1.2), a photoconductive switch (Section 1.2.2.1), or a non-linear medium (Section 1.2.2.2). These devices are generally used to produce the THz pulses and will be covered in detail in Section 1.2.2.

A frequency down-conversion method to produce CW THz is one of the most used for THz spectroscopy and is called photomixing. The generation of THz with photomixing relies on the coupling of two IR lasers which are slightly detuned. By precisely controlling the wavelengths of

the pump lasers with their temperature, the difference in their frequency will produce an intensity beat in the signal. This beat will then be focused on the photomixer, where it will induce a photocurrent. This current will ultimately be directed toward an antenna that will produce the free space THz generation [1]. On the one hand, this technique has the advantage of generating a uniform THz power on a wide spectrum (between 0 and 1.8 THz) [19], but on the other hand, it is very limited in its output power by the efficacy of the photomixer. The optical-to-THz conversion ratio is typically in the range of 10^{-6}-10^{-5} [1]. This efficiency drops when trying to produce high frequencies, i.e., when the two IR laser frequencies are the closest to each other. Nevertheless, it is one of the most precise ways to tune THz waves, and one of the oldest.

2.2.1.4. Vacuum electronic sources

The final category covers some sophisticated vacuum THz sources, such as gyrotrons, Klystrons, or travelling-wave tubes (TWT) [20]. These sources are typically rarer and more expensive, but their high output power (some of these sources can produce up to GW of optical power) and wide range of emission (from 0.1 to 10 THz) makes them unique and very attractive for many applications. Although often categorized together, they generate THz with a wide range of mechanisms. A complete description of their working principles can be found in reference [31], but for imaging purposes, this thesis will rather focus on the backward-wave oscillator (BWO) or carcinotron, which is used in multiple interesting setups of THz imaging. The BWO is a device that is part of the TWT family. It was first invented in 1950 and used for THz imaging in 2004 [32]. It distinguishes itself from other sources by its power and high spectral resolution. Its generation of essentially monochromatic and stable THz radiation makes it rather easy to align in a system. When focused, it enables good spatial resolution for imaging and spectroscopy with a high signal-to-noise ratio (SNR).

Its working principle consists in producing a relativistic electron beam confined by a strong magnetic field in the vacuum. The electron beam is directed from the electron gun to the anode at the other end of a tube. The beam interacts with a helical conducting structure acting as a slow-wave structure (SWS). This SWS is a periodic pattern that “slows” the electron beam when it intersects it. This pattern generates a wave moving in the opposite direction to the beam (from the anode to the electron gun) and whose frequency is determined by the group velocity of the opposite wave. This group velocity is tuned by the voltage difference between the gun and the SWS, and

the geometry of the SWS. BWO output frequency is typically below 1 THz, and their output power can reach a few dozens of mW.

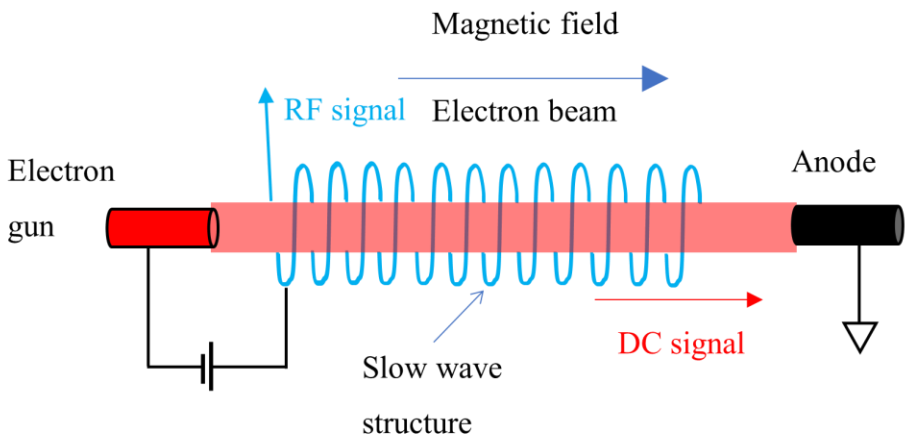

Figure 2-4: Schematic of the working principle of a BWO.

Since 2004, many imaging applications use a BWO to generate the THz illumination. The high quality of the signal made them ideal to test the diffraction limit in THz imaging and to find solutions to improve it [33,34].

2.2.2. Generation of pulsed THz

Although CW sources have a high spectral resolution, their speed of acquisition of an image remains a downside of this imaging technology. That is why imaging with pulses is often a preferred way for many applications. In the THz range, a pulse should typically last between one and a few dozens of picoseconds, which has been for a long time the limit of the electronic sources. It is the invention of the femtosecond laser Ti:Sapphire that changed the situation in 1982. A femtosecond pulse used with frequency down-conversion system is what enables the main sources of picosecond pulses in most imaging systems nowadays. The next section will address three of these sources, which are the most covered in the literature.

2.2.2.1. Photoconductive antennas

The effect of a photoconductive switch consisting in a thin slab of high-resistivity silicon activated by an ultrafast pulse of light was first observed in the Bell Laboratories in 1975 [35]. By then, it was described as a novel way to manipulate electrical signals in the field of electronics. A few microjoules of radiation were emitted in 15 ps with the potential to reduce the impulsion time even further. A few years later, the air transmission of a 1.6 ps impulsion was observed in the same lab, this time by illuminating a Hertzian dipole with a pulse of light produced by a mode-locked laser [36]. It was the first report of a photoconductive antenna (PCA) capable of generating and detecting THz, which is still to this day one of the preferred ways of producing clean pulses of THz.

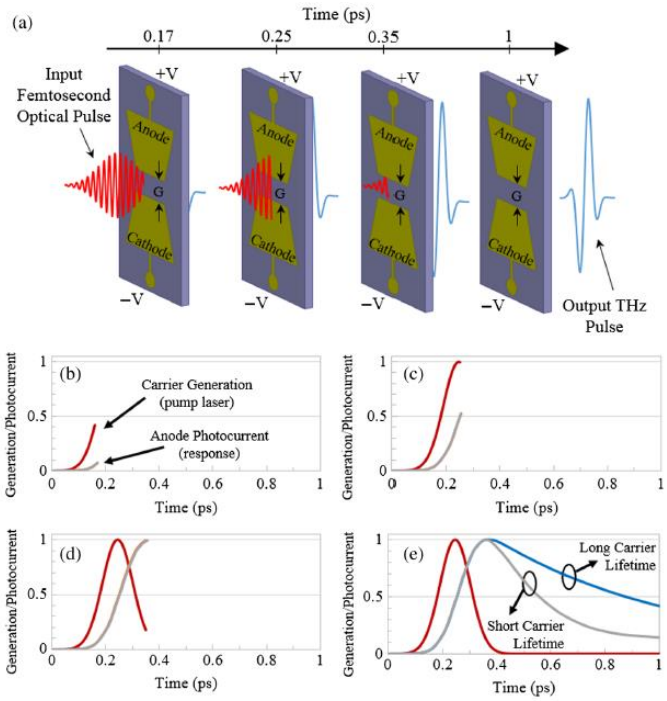

Figure 2-5: a) Schematic of a photoconductive antenna working principle. b), c), d), and e) show the time evolution of carrier density and anode photocurrent for different time frames of the activation of the antenna by a light pulse. Reproduced from [37]

The principle of a PCA is straightforward: an anode and a cathode are deposited on a semiconductor slab with a gap between them. A voltage is applied between the anode and the cathode so that the semiconductor blocks the flow of current in the gap. However, when a pulse of light is focused on the gap, it generates a carrier density that immediately allows the current to flow between the electrodes for the duration of the pulse's travel through the slab (see Figure 2-5).

Multiple parameters need to be set carefully to optimize the performance of the PCA. First, the type of semiconductor determines the optical wavelength that activates the switch and the carrier lifetime (which must be short to produce shorter pulses). Many other properties also need to be considered, such as the carrier mobility, the bandgap shape, the breakdown voltage, and the suppression of zero bias photocurrent, among others [37]. All of these considerations make gallium arsenide (GaAs) and indium aluminum arsenide (InAlAs) to be the most used semiconductors in modern PCAs. GaAs bandgap is activated by an 871 nm wavelength, making it perfectly suited for Ti:Sapphire femtosecond mode-locked lasers.

2.2.2.2. Non-linear optics

Non-linear optics refers to the branch of optics in which light pulses are powerful enough to observe non-linear behaviours in the polarization induced in a medium. In a first approximation, polarization is typically considered to be a linear function, as is seen in Equation 2-5

$$\vec{P} = \epsilon_0 \chi \vec{E} \qquad (2-5)$$

where P is the polarization, ϵ_0 is the vacuum permittivity, χ the material susceptibility (real number), and E the electric field [21]. While this is true for low electric field intensity, some materials start to exhibit non-linearity under a higher intensity, i.e., χ becomes a tensor and the polarizability generates an electric output that can be modulated. The conditions to observe this behaviour are typically met when using an ultrashort pulse as a pump, such as the one produced by Ti:Sapphire femtosecond mode-locked lasers. Using the right crystal, different setups can be used to generate THz using non-linear optics, such as the second order non-linearity optical rectification [38] or third-order non-linearity frequency mixing [39]. Especially for electro-optic sampling, these techniques can produce THz pulses with a large bandwidth for most imaging applications. It is in this sense less limited than the PCAs which emit at a resonance frequency of twice their dipole length [40]. Their imaging applications are promising, although the alignment is difficult and the sensibility of the detection is low [41].

2.2.2.3. Plasma systems

Another THz emission method based on a non-linear effect that is currently attracting a lot of attention is the two-color plasma. These THz pulses were first reported in the 1990s when studying the plasma produced by four-wave mixing. This phenomenon in itself is difficult to produce, as it needs to focus a laser femtosecond pulse with its second harmonic produced by a BBO crystal. These experimental setups use a Ti:Sapphire laser of 800 nm with the 400 nm second harmonic. The interaction of both pulses produces a plasma emitting broadband THz pulse, whose amplitude increases with the optical power of the pulses [42]. Recent progress could simplify the experimental setup by confining the plasma in a THz waveguide [43], but the resulting pulse amplitude is reduced. Some reports propose improvement by changing the pump wavelength with an optical parametric amplifier (OPA) to optimize the resulting THz pulse, which could make plasma a more practical source for THz application [44].

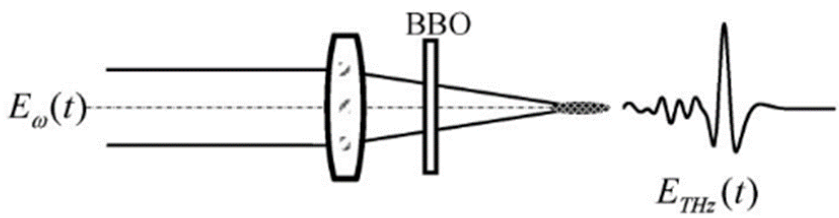

Figure 2-6: Schematic of the common setup for the four-wave mixing in the air plasma that can be used as a mechanism of THz wave generation. Reproduced from [42]

2.2.3. Some applications of THz imaging

As we saw in Figure 2-2, interest in THz imaging increased drastically since the 2000s, as the specialized imaging laboratories refined their control on THz generation. The first THz time-domain-spectroscopy (THz-TDS) system was built in the Bell Laboratories in 1995, with PCA as both the THz source and detector [45]. The demonstration that time-domain-spectroscopy could be extended from the traditional range of IR to the new one of THz was significant, and the same setup was reproduced by many scientists to see how THz would perform in traditional applications of imaging. Here, we present a few examples of such applications and the THz system

performances. For more details on the field, many literature reviews can be consulted, such as the one in reference [46].

2.2.3.1. Spectroscopy

From an optical point of view, one of the first incentives to study THz came from the need to extend the IR spectroscopy band. This also motivated the development of THz detectors capable of coherent detection, meaning that the detector would be sensible enough to detect the phase and the amplitude of the EM wave.

The upside of using THz waves in spectroscopy is multi-faceted. One such upside is due to their strong absorption with polar molecules such as water which becomes practical in the study of α-lactose monohydrate in reference [19]. Another upside is in the detection of weak noncovalent bonds like the hydrogen bond and the van der Waals forces in reference [47]. In either case, a precise THz system can yield a better measure of the spectrum of absorption of the sample, which is then used for its identification. For example, the spectra of water in the THz range has gathered attention since the discovery of THz, since this part of the spectrum could achieve a better SNR over the thermal background than in the IR while maintaining a better precision on the line strength than in the millimeter-waves range [48].

With broad frequency ranges like the THz, coherent detection is technically difficult to achieve as it requires a high spectral resolution. It can be realized either by moving the phase incrementally with a delay line or by scanning an interference pattern in the intensity of the transmitted power [19]. The THz spectroscopy system can use either a CW or a pulsed source. In general, it can be said that CW setups have a better spectral resolution, while pulsed setups have a quicker time of acquisition. The spectral resolution of such a system being much more important than its spatial resolution, this application is not considered to be affected by the diffraction limit. Nevertheless, spectroscopy does benefit from a better focus to isolate the spectrum of details on a sample.

2.2.3.2. Semiconductor imaging

The precise characterization of the dielectric function of a material can also be crucial in the semiconductor industry, either to choose materials in the design of new devices or in the post-fabrication verification of the device's function. Typically, properties of conductors such as carrier

lifetime, mobilities, and dopant concentrations, are characterized by the Hall effect measurements. However, this technique is inapplicable in the case of nanowires, which are becoming more and more important in modern electronics because of their one-dimensional nature [49]. It also appears that the mechanism of THz relaxation can explain approximately 15 to 17% of the value of low-frequency dielectric constant, as studied on organosilicate glasses in reference [50]. Both examples are related to problems that modern electronics need to overcome in the near future, and both show a clear upside to using THz technologies.

These applications, especially for the study of nanowires, are very limited by Abbe's resolution limit. Nanowires are typically less than 300 nm long, which is much smaller than the diffraction limit of 150 μm at 1 THz. In general, the study of semiconductors would require an improvement in the resolution of THz systems of three orders of magnitude to unlock the full potential of the technique, which would be a very remarkable feat.

2.2.3.3. Medicine

As discussed previously, THz are strongly absorbed by water and their absorption lines are very well documented in the literature. This feature in itself gives THz interesting prospects in medicine and cancer prevention, since tumors often indirectly cause water content to increase in some tissues [51]. Because of this feature, THz can also be used to monitor the formation of ice during cryosurgery, a novel technique that consists in freezing tissues to remove them or differentiate them from other tissues [52]. Additionally, the low photon energy of THz is insufficient to cause ionization, which makes it safer to use for non-invasive biomedical imaging, unlike X-rays and γ-rays [5]. This field of application for THz is extremely recent, but also gives a direct path for THz to be adopted in new technologies.

As medicine and biomedical imaging progresses, it becomes obvious that THz have a role to play in this ever-expanding field. As the penetration depth seems like a workable problem [53], the diffraction limit remains an important obstacle to overcome, as shown by the use of THz microscopy in the study of a rat glioma model in reference [54]. In this study, a resolution just a few times below the diffraction limit gives enough details to distinguish important features in the rat's brain, showing a good first application of THz super-resolution in medicine.

2.2.3.4. Security

The combination of safe radiation for humans (operator and target) and good resolution that makes THz interesting in medicine also happens to make them appealing for security purposes. In addition to that, the very low absorption of THz in non-polar and non-conducting elements, which applies to most fabrics, papers, and plastics, makes them perfectly suited to detect weapons or explosives concealed on people or in packages [55]. In reference [56], the authors note that many common explosives like 2,4,6-trinitrotoluene (TNT), hexahydro-1,3,5-trinitro-1,3,5-triazine (RDX), tetramethylene tetranitramine (HMX), pentaerythritol tetranitrate (PETN), PE-4, and Semtex have noticeable absorption fingerprints below 3 THz due to lattice vibrational modes of solid-state explosive materials. The detection of illegal drugs or toxic chemicals could also be possible with THz spectroscopy, providing a quicker and simpler way to analyze unknown substances for security purposes [57].

The security applications of THz do not require a very specific resolution, but would still benefit from details at a subwavelength size (100 μm at 3 THz). Similar to applications in medicine, an order of magnitude smaller than the wavelength would be a satisfying resolution for this field.

Table 2-1 shows a summary of the applications of THz microscopy that we introduced in this chapter and the resolution that we estimated. The resolutions are of course mere estimates and are not meant to underscore the interest in achieving THz nanoscopy. It must be appreciated, however, that the THz wavelengths can be much longer than the details they are meant to resolve. Furthermore, although all these resolutions are possible to achieve, the systems that do are often limited by other practical factors, as we will see in the next section.

Table 2-1: Potential applications of THz microscopy and the estimation of resolution required.

Application	**Resolution**
Spectroscopy	$10^{0}\ \lambda$
Semiconductors	$10^{-3}\ \lambda$
Medicine	$10^{-1}\ \lambda$
Security	$10^{-1}\ \lambda$

2.3. Solid immersion imaging

In terms of THz imaging, the main observation derived from Section 1.2 is that the long THz wavelengths are a significant physical limitation for their potential applications. It is not a surprise therefore that overcoming the diffraction limit in resolution attracted so much attention over the years. This section will be devoted to the imaging systems achieving super-resolution. First, we present the highest standards in microscopy and an overview of the highest resolutions reached by non-THz imaging systems not limited by diffraction. Then, we touch on the subject of near-field imaging, a type of system that achieves direct super-resolution, regardless of the wavelength of operation. Finally, we introduce the solid immersion system and its unique way of overcoming the resolution limit.

2.3.1. Some solutions to the diffraction problem

It must be appreciated that for many applications, the diffraction limit does not pose a problem because super-resolution is not needed. For example, X-rays used in laminographic imaging mode, because of their shorter wavelengths, yield a resolution of a few hundred nanometers, which is more than enough for most applications in medicine [58]. The Blue light (405 nm) used in blu-ray disc readers gives a precision high enough to image at high-speed bits of 476 nm, which is competitive in terms of data storage technologies [59]. Even though X-rays' impacts on the target's health are concerning, and Blu-ray discs are quickly being replaced by solid-state data storage systems, using shorter wavelengths might be the easiest way to improve the resolution of a system if the application is flexible on that matter.

In some other cases, super-resolution is achieved by other means that avoid using the spot size of a focused beam as a measure of resolution. Fluorescence microscopy is an interesting case in the biomedical field. Its resolution does not consist in focusing the illuminating light on a spot and registering the transmission/reflection response, like in conventional microscopy, but in focusing an illuminating light and recollecting the fluorescence emitted by a marker (dye) that was previously injected in the region of interest (ROI). In such a system, the definition of resolution changes. Instead of being defined by the ability to distinguish two features on the sample, it is

instead defined by the ability to see contrast between the labels used within a diffraction-limited spot size [60]. In that sense, many authors have reportedly clearly broken the diffraction limit with fluorescence systems [15]. Resolution as high as 10 nm with visible wavelengths and single-molecule imaging has been reported in reference [61]. However, this imaging technique is limited in its application (it is more common in *in vivo* imaging), and the precision of its results also needs to be interpreted within the limitations of the system. The concept of labeling can be further refined when using dyes with a non-linear response. In the example of two-photon microscopy, the fluorescence excitation is based on a second-order non-linear response of the material (as discussed in Section 1.2.2.2) called two-photon absorption. This phenomenon occurs when two photons are absorbed simultaneously by the dye, which emits back one photon with the combined energy of the other two. This condition being only met at the point of maximal intensity in a focused femtosecond laser beam, it is possible to locate the ROI with a precision much higher than normal fluorescence microscopy [62]. This technique has already yielded good results during trials of brain surgery on mice [63].

The gold standard in nanoscopy to this day is still the scanning electron microscope (SEM) and the atomic force microscope (AFM). The first probes the surface of the sample with a beam of electrons generated in a vacuum chamber [64], while the second uses a probe to detect the changes in the topology of the sample to produce an image [65]. Both techniques bypass the diffraction limit by probing the surface of the sample instead of imaging with focused EM waves. They both achieve ultra-high resolution of a few nanometers. They are costly, however, and limited in their applications. For example, the SEM can only image conducting materials. They are also limited to imaging the surface of the sample and have very little penetration depth. Image acquisition can also be very long due to their conditions of operation (vacuum and low temperatures).

To remain within the scope of this thesis, other techniques will not be explored further. However, one technique that is extremely relevant to the super-resolution field and needs to be introduced is the Near-field imaging.

2.3.2. Near-field imaging

As a general definition, the NF imaging systems are designed to use the interaction between illuminating light and the sample in its "near-field" region, i.e., at a distance of less than a wavelength. In this region, the pattern of interference has not yet fully deteriorated the initial wavefront and information can still be extracted from subwavelength areas. These techniques are heavily documented and have delivered some of the best resolutions in the literature. Their downside is the complexity of the setup, which does not fit just any sample or application, as well as the time of acquisition which makes it difficult to achieve real-time imaging [22]. Additionally, the penetration depth of these systems is typically low, as it cannot be more than a few wavelengths. However, their principles are simple, which allows a flexible implementation for different applications. There are two main types of NF imaging systems: with aperture and without aperture.

2.3.2.1. NF imaging with aperture

The most direct system of NF imaging consists in doing the experiment tried by Toraldo di Francia and described above, which uses a subwavelength aperture in the propagation plan of the illumination beam. This aperture is placed in the NF region of the sample, and therefore acts as a very small source of illumination for the sample and can image a subwavelength volume. This imaging system is often referred to as scanning near-field optical microscope (SNOM) [66]. Such a system, although being theoretically free from diffraction, has the large disadvantage of having power absorption proportional to a^6, where a is the radius of the aperture [67]. This limitation makes this system mostly convenient for systems with very powerful sources. Moreover, the image acquisition with this system can be very slow, making it very inconvenient for applications needing real-time imaging [68]. SNOM systems were built for different applications, yielding a vast range of resolutions, from λ/5 [69] to λ/50 [70]. In terms of THz imaging, reports of improved PCAs with extreme sensibility given by resonant cavity could yield very high resolutions down to λ/150 despite the low power of the signal [71].

2.3.2.2. Apertureless NF systems

The apertureless version of a SNOM is called a scattering-type scanning near-field optical microscope (s-SNOM). Like the SNOM, a s-SNOM works by collecting light interaction in the NF of the sample to image smaller points than the diffraction limit at the wavelength used. However, to avoid the very high loss of power of sub-wavelength aperture, the apertureless SNOM instead uses a metallic tip to probe the surface of the sample (which is reminiscent of the AFM) [72]. An illuminating pulse of light is polarized and focused on the region of interaction of the probe sample. The concentration of electric field at the apex of the tip is therefore confined between it and the sample, and back-scattered light carries information from both the local dielectric properties of the sample and the probe-sample distance [73]. To isolate the sample information, this distance (typically a few dozens of nanometers) is modulated by the probe oscillation at its mechanical frequency Ω. A lock-in detector placed in the far-field samples the scattered signal at a non-fundamental harmonic of Ω, reconstructing the image of the sample. The s-SNOM is almost limitless in terms of resolution. Only in the last few years, many authors reported the fabrication of such systems for THz imaging with resolution down to 10^{-3} λ [73,74].

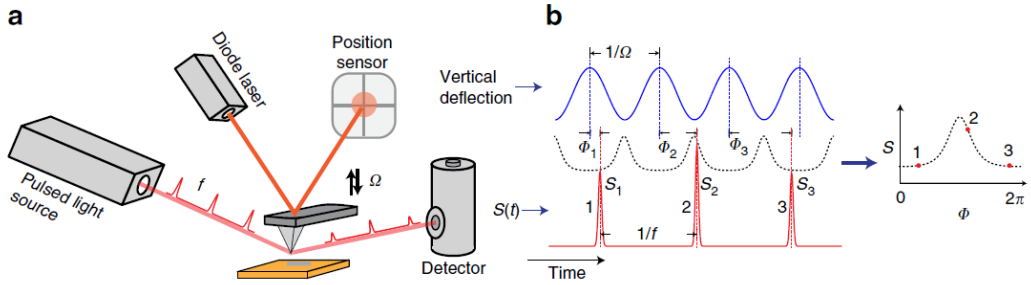

Figure 2-7: a) Schematic of a s-SNOM. b) Representation of the reconstruction of the topography of a sample with a s-SNOM. The blue line represents the oscillation of the tip and the red line represents the pulses of light focused on the tip at different positions. Reproduced from [75].

2.3.3. Solid immersion systems

Even before Abbe's work on microscopes, a specific parameter that could improve the resolution had been identified by many microscope manufacturers. This parameter is the RI of the medium surrounding the image plane. Indeed, by 1840, Giovan Battista Amici had already produced a water immersion microscope objective [8]. The increase of RI between water and air (1.3 vs 1) would slightly improve the resolution by confining the beam of light illuminating the sample at λ/n, where n is the RI of the medium. Later, oil would replace water (1.5 vs 1.3) and provide even better results. 150 years later, Mansfield and Kino reported the fabrication of a microscope (see Figure 2-8) working on a very similar principle, although using a hemispherical lens of $n = 3.5$ in the NF of the sample rather than immersing it in liquid [6]. Such a system would also increase resolution by a factor of n. This system had a much better light budget than SNOM while producing an image directly observable in real-time.

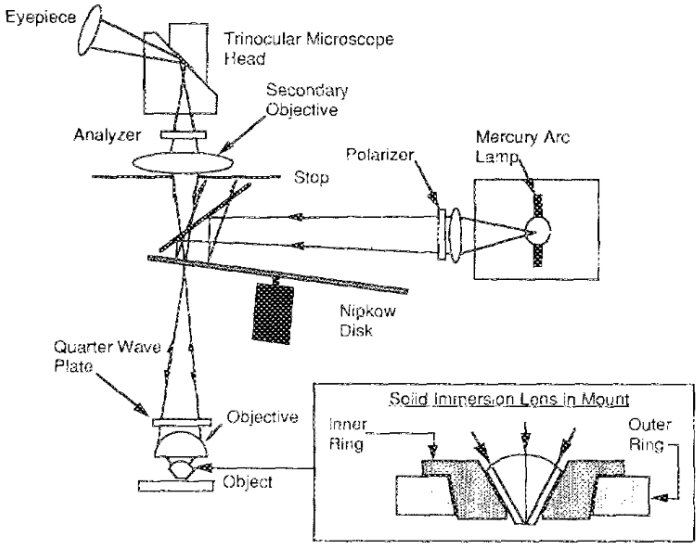

Figure 2-8: Schematic of the first solid immersion microscope built by Mansfield and Kino. Reproduced from [6] .

Solid immersion lenses became a very dynamic field of study shortly after. Many groups started testing different shapes of lenses, such as superhemispherical lenses (like the Weierstrass' lens, whose geometry improves resolution to the cost of chromatic abberations) [76, 77], cuboid lenses [78], or aplanatic lenses [79] using hyperbolic metamaterials [80] and microspheres [81], among

others. Unlike the SNOM and s-SNOM, this imaging system has a very strong light throughput, making it practical for applications with limited optical power.

When applied to THz imaging, an additional upside of the solid immersion system is that the RI of the materials is typically higher in the THz range than in the visible. It is therefore very possible to find ways to produce THz SILs with a refractive index of around 3.5 or higher, especially using ceramics such as titanium dioxide (TiO_2) [82, 83]. Furthermore, research in the past few years on the design of high-RI metamaterials in this region has reported RIs as high as 67.9 (polarization-independent) [84], and as high as 100 (polarization-dependent) [85]. Such materials are fabricated by the deposition of a conductor layer on a dielectric substrate in such a shape that it reaches resonance at a chosen frequency. These materials have therefore a very short bandwidth on which the RI is as high as reported. Their fabrication is noteworthy nevertheless and could show progress in the field of SILs.

The fabrication of solid immersion imaging systems has already been reported in the THz range and slightly above by many groups [33, 34, 54, 86-89]. These results and important details of the systems are presented in Table 2-2 along with the application for which they were built. A clear conclusion from the table is that solid immersion imaging is still much more limited in resolution than the SNOM and the scattering NF systems. The reported results are nevertheless in the range of the applications discussed in Section 1.2.3 while offering many advantages compared to the SNOM and s-SNOM. In the case of these systems, the use of the term “super-resolution” is debatable, since the wavelength of illumination light itself is changed by the propagation through a high RI medium. It remains however a very practical solution for imaging below the diffraction limit in air.

From Table 2-2, we can also observe that until now, most tested SILs are in high-resistivity float-zone silicon. This material is interesting for the fabrication of SILs since its RI in the mid-IR and THz range is high (~3.5), but lenses in this material are expensive and hard to fabricate. Improving the fabrication of SILs is therefore a relevant goal to test the full potential of solid immersion imaging.

Table 2-2: Compilation of Solid Immersion Systems and their final resolution reported.

ν [THz]	RI (material)	Resolution	Application	Ref.
0.1 – 0.2	3.1 (Sapphire)	0.3 λ	N/A	[86]
60	3.43 (Si)	0.28 λ	Thermal microscopy	[87]
28	3.4 (Si)	0.23 λ	N/A	[88]
0.5	3.42 (Si)	0.35 λ	N/A	[34]
0.3 – 1.4	3.5 (Si)	0.49 λ	Spectroscopy	[89]
250	3.5 (Si)	0.29 λ	Semiconductor imaging	[90]
0.6	3.42 (Si)	0.15 λ	Medicine	[54]

2.4. Possible methods for SIL fabrication

As explained in Section 1.2, the design of THz optical systems needs to reduce as much as possible the absorption because of the limitation in power generated by the sources. Therefore, it is typically preferred to use reflecting elements rather than refractive ones. When it is necessary, refractive elements in THz, such as lenses, are typically made of plastic and machined on a lathe, as is often the case for other optical components in the IR/visible spectrum [20]. Polymers such as Polypropylene (PP), High-Density Polyethylene (HDPE), or Teflon (PTFE) are excellent materials for THz refractive components as they have a very stable RI on a wide bandwidth and low absorption losses [91]. As this project focuses on refractive lenses with very high RI, the fabrication techniques will be chosen so that TiO_2, one of the elements with the highest RI in THz, can be an essential part of it. In this section, some of the techniques used in the literature to fabricate optical components will be presented and compared in terms of their abilities to create high refractive index components.

2.4.1. Hot press

The simplest way to fabricate a solid structure with two elements is by pressing. Such a strategy was the one recommended in the report [92], and a study of the refractive index of a TiO_2-doped polymer had been discussed in reference [93]. The method consists in compacting TiO_2 powder in

a mold with another material powder, like a polymer, that would serve as a “glue” to keep the lens solid. To create the best structure, the pressing needs to be made at the Vicat temperature, a temperature at which the polymer softens enough to be penetrated by the TiO_2 particles, but not enough to become liquid [94]. This technique is inexpensive and very easy to implement. The lens fabricated would however be porous, which would decrease its effective refractive index.

2.4.2. Sintering

Sintering is another technique using a hot press, but at much higher pressing parameters. It consists in pressing the pure TiO_2 powder at high pressure and temperature so that new connexions are made between the different crystalline particles, producing a solid structure made of all the particles. Sintering of TiO_2 has been reported to yield structures with densities up to 99% [95], and very high dielectric constants (i.e., high RI) [96]. The parameters of this process are the TiO_2 particle size, the temperature of the press, and the pressure applied. TiO_2 particles need to be very submicrometric (a few dozens of nm), and if possible, in the same crystalline phase (a mix of rutile and anatase is the most common). The powder preparation process varies between the studies, and can include preliminary compression steps like cold isostatic pressing [96] or dispersion in aqueous solutions [95]. The temperature and pressure applied during the sintering will influence the size of the grains inside the sintered lens. Typical temperatures can range from 700°C to 1,250°C with pressure between 0 and 80 MPa [83], but sintering was reported to a temperature as low as 400°C at a pressure of 1.5 GPa [97]. In reference [83], the waveguiding properties of titanium ceramics for millimeter-waves are studied. A very high dielectric permittivity of 90 (RI of approximately 9.5) is observed, although the authors also note that the inclusion of impurities in the powder influences significantly the losses of the structures.

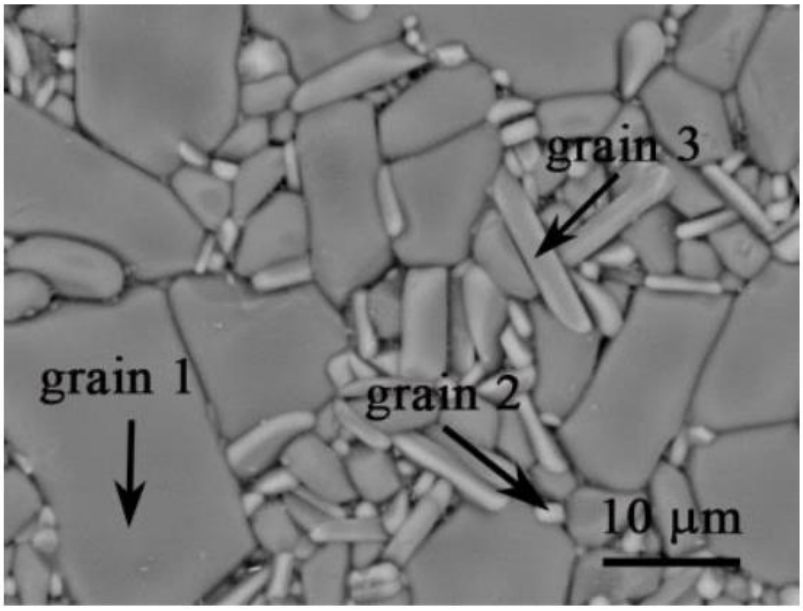

Figure 2-9: SEM picture of a ceramic of 0.95 MgTiO3 – 0.05CaTiO3 sintered at 1,300 °C. Reproduced from [83].

2.4.3. 3D printers

Additive manufacturing is rapidly becoming a normal strategy for customized optical components, and it is mainly thanks to the emergence of highly efficient and cheap 3D printers. 3D printer is a term used to regroup multiple additive manufacturing machines working with different principles such as stereolithography [98] and selective laser sintering [99]. One of the most commonly used and convenient printers remains those using melting deposition, also called fused layer modeling (FLM), fused filament fabrication (FFF), or fused deposition modeling (FDM). These printers use polymer filament (a very wide range of polymers are available) that they melt and depose layer after layer to make 3D constructions. The precision of these printers has greatly improved over the years due to a better control of parameters such as nozzle temperature, heatbed temperature, printing speed, and nozzle height, among others [100].

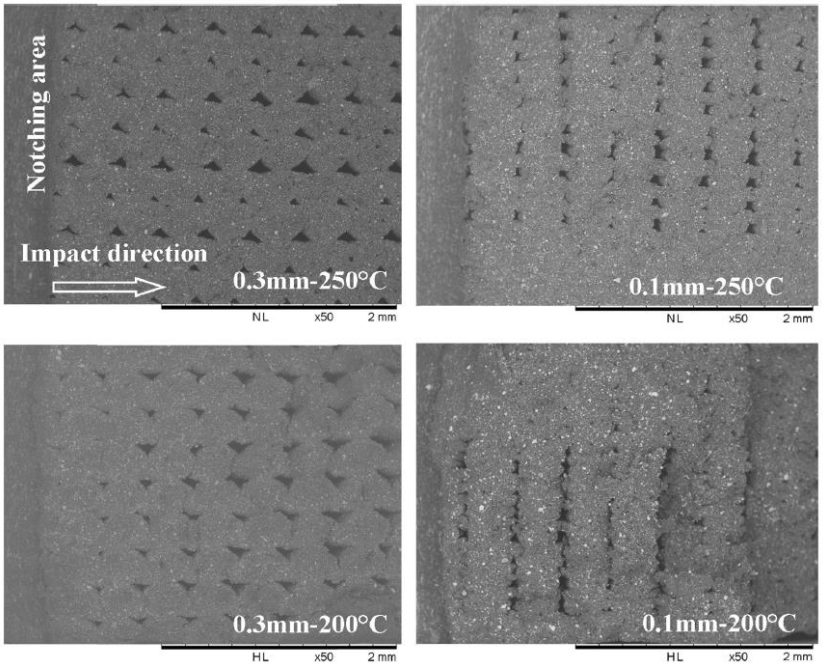

Figure 2-10: Pictures of cryo-fractured surfaces of 3D printed structures with PP at 0.1 mm of layer height. The pictures show the variation of density between each filament deposed. Reproduced from [101].

In the THz band, they become particularly interesting due to their ability to print waveguides with subwavelength details in low-loss plastics very quickly and with high repeatability, which is very convenient for the research and development of waveguides [102]. Some researchers also reported on the possibility of customizing the filaments used in 3D printers by adding inclusions of other materials in the plastic. In reference [103], the inclusion of glass in PP allows the modulation of different mechanical and physical properties of the printed structures. In reference [104], TiO_2 particles are inserted in a PP filament to change the mechanical and optical properties such as the RI of devices fabricated for medical applications. However, the highest percentage of TiO_2 inclusions tested is very low (4% of weight), which does not significantly affect the RI.

2.4.4. Sol-gel

Sol-gel is a chemical procedure in which a colloidal solution is brought to the solid (gel) state by the formation of a gel. This method is known for being efficient at creating hybrids of metal-oxides and organic compounds [105]. The design of a sol-gel structure depends mainly on the precursors, i.e., the solutions in which the particles that have to solidify are initially mixed. Sol-gels of TiO_2 are very common, although most of their applications are with thin film rather than large 3D structures [106]. Nevertheless, some reports can be found on the fabrication of small lenses fabricated by the sol-gel process of TiO_2 [107, 108]. In reference [108], the resulting lenses have a radius of approximately 2 cm and a RI of approximately 1.45. The low refractive index is mainly due to the low concentration of TiO_2 within the gel (which is rather porous). This technique typically offers an excellent homogeneity in the dispersion of TiO_2.

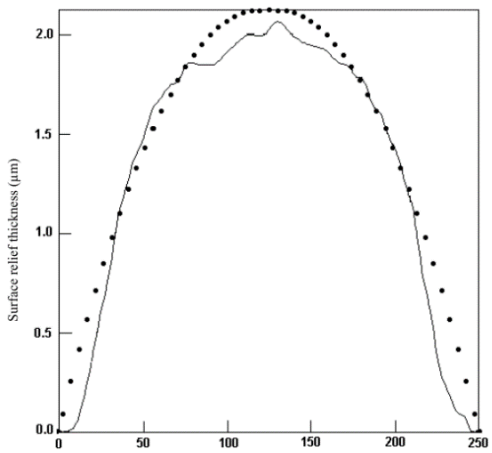

Figure 2-11: Profile of the surface of a microlens fabricated in SiO_2/TiO_2 sol-gel. Reproduced from [107].

2.4.5. Epitaxial growth and other deposition techniques

The final technique reviewed in this section is the growth of single-crystalline TiO_2 structures by epitaxial growth or magnetron sputtering. This fabrication technique consists in growing a cylinder of pure TiO_2 crystal in the rutile form (its most common) that could then be cut and polished into a hemispherical shape. In reference [109], magnetron sputtering is used to produce a film of rutile and anatase TiO_2. The refractive index calculated shows that the 150 nm thick film has the RI of pure TiO_2, meaning that the film has an ideal concentration. In reference [110], magnetron

sputtering is used for the nanoarchitecture of nanorods of a few hundreds of nanometers. In 2019, a group managed to grow a porous single crystalline structure in TiO_2 of 10 mm x 20 mm x 0.5 mm, demonstrating that components could eventually be built with this material in a crystalline form [111].

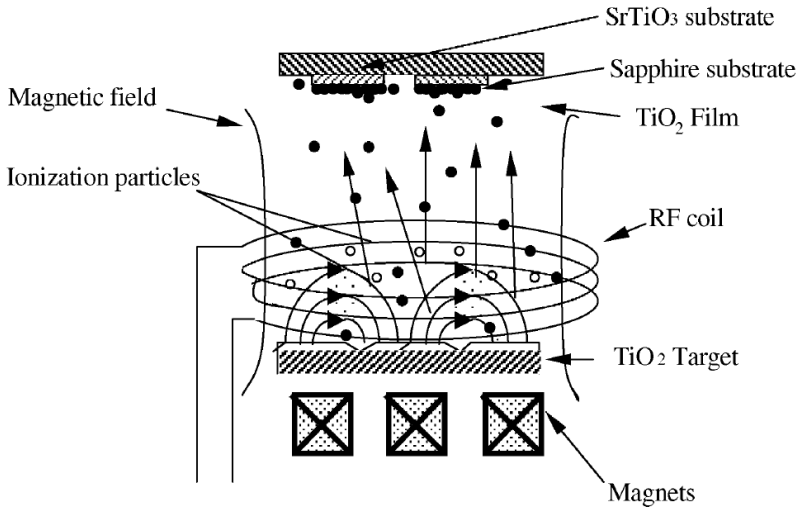

Figure 2-12: Schematic diagram of a helicon magnetron sputtering cathode used to grow a TiO_2 film. Reproduced from [109].

CHAPTER 3 METHODOLOGY

3.1. Choices in the design and materials

This project started with the preparation of the unpublished report in 2019 "*Étude sur les composites céramiques-polymères pour l'imagerie THz par immersion solide*" [92]. The objective of this research project was to identify materials that could be used to fabricate SILs for THz imaging. In its conclusion, the author strongly recommended the use of TiO_2 and PP powders as materials to achieve high RI pressed lenses. Among other reasons, the low cost of both materials and the simplicity of fabrication would quickly produce lenses that could be tested and characterized. TiO_2 is chosen for its high RI in the THz wavelengths and PP is chosen for its very low absorption in the THz wavelengths.

TiO_2 is indeed a very interesting material for optical components in THz. Its refractive index is evaluated to 10 [112] and is available in multiple shapes, although its most common one is as a powder [113]. As presented in Section 1.4, powders can be a very convenient material to fabricate material components, as they can be used either in molding, 3D printing, or sol-gel techniques. To achieve the highest refractive index, however, TiO_2 needed to be as compact as possible in the final hemisphere. To that end, it appears obvious that pressing the powder would be the best technique available. The low absorption coefficient of PP makes it a very convenient secondary material to shape the TiO_2.

We used the Bruggeman model for effective media to make a theoretical prediction of the RI achievable for our fabricated SILs. In this model, we account for a composite SIL with inclusions of TiO_2, PP, and air (to account for the porosity). Indeed, porosity can be a determining factor in the hot press technique. Unlike sintering, the particles will not recreate new connexions between each other, and therefore, space will be left between them. The model consists in numerically solving the equation

$$f_{air}\frac{n_{air}-n_{eff}}{n_{air}+2\cdot n_{eff}}+f_{TiO_2}\frac{n_{TiO_2}-n_{eff}}{n_{TiO_2}+2\cdot n_{eff}}+f_{PP}\frac{n_{PP}-n_{eff}}{n_{PP}+2\cdot n_{eff}}=0 \qquad (3-1)$$

where n_{air}, n_{TiO2} and n_{PP} are the RI of air (1), PP (1.510) and TiO_2 (10), and f_{air}, f_{TiO2} and f_{PP} are the volume fraction occupied by each of the inclusions. First, different mixes of TiO_2 powder and PP powder are made with different weight concentrations of TiO_2: 85.6%, 90.2%, and 94.1%. The fractions can be transformed into filling factors through the density of TiO_2 (4.23 g/cm^3) and PP (1.07 g/cm^3). We plot the effective RI of each mix while varying the porosity factor. We also plot the RI of a powder mix that would be exclusively made of porous TiO_2 (see Figure 4-14). This last concentration will be tested in a different model of SIL in which we use a 3D printer to fabricate a thin shell in PP and in which we manually press pure TiO_2 powder. In the submitted paper presented in the next chapter, every step in the fabrication process will be described in more detail.

3.2. Characterization of the SILs

The next step of the project was to characterize and test the resolution of each fabricated SIL. The characterization of the RI was made with a cutback measurement. This technique (well documented in reference [114]) consists in stacking thin slabs of a material to characterize, and then measuring the electric field amplitude and phase of an EM wave traveling through the stack. When removing the slabs one after the other, the distance traveled by the wave inside of the material varies, and it is possible to calculate the complex RI of the material. The setup of the cutback system used for this project is presented in Figure 4-12. The RI should theoretically give an idea of the improvement factor in the resolution of the reflection-based time-resolved solid immersion microscope. Next, we present the fabrication step of this microscope and its alignment.

3.3. The solid immersion system

3.3.1. Producing the THz pulse

The microscope built for this project is based on a THz-TDS system that was previously built by Hichem Guerboukha, Ph.D. In the setup presented in Figure 4-6, a femtosecond pulse centered around 800 nm produced by a Mai Tai Laser (from Spectra-Physics) is divided in two by the BS2. The first pulse is sent directly to the THz detector, a PCA produced by Menlo (TERA8-1), in a part

of the setup called the detector arm. The second pulse is sent to the THz transmitter, an interdigital array PCA fabricated by Batop Optoelectronics (iPCA-21-05-1000-800-h), in a part of the setup called the transmitter arm. On the transmitter arm, the pulse travels in a delay line that allows us to control the time-of-flight of the pulse. The IR pulse in the detector arm generates a THz pulse in the Batop PCA following the mechanism described in Section 1.2.2.1. The THz pulse is reconstructed by lock-in detection at the Menlo PCA, by measuring the electric field for different positions of the delay line. The time position of the reconstructed pulse is determined by the time-of-flight of the pulse depending on the delay line position. For the detection to work, the distance in the detector arm must be approximately equal to the distance in the emitter arm. The delay line consists in a motorized stage (Thorlabs DDS220 direct drive stage) moving at 45 mm s^{-1} on 20 mm. The acquisition card records 1 753 measures of the electric field at 2 500 Hz during the motion of the delay line to reconstruct a THz pulse of approximately 120 picoseconds.

In the first alignment step, the detector is placed on a 3D motorized stage (three Thorlabs LTS300 translation stage) allowing positioning of the detector in space with a precision smaller than 3 µm. The propagation axis of the pulse is defined as the z-axis. The detector can be moved in the x and y-axes to characterize the shape of the beam at every position along the z-axis. To align the system, the L1 lens must be positioned to assure a perfectly collimated beam between L1 and L2. L2 is therefore removed, and the beam is scanned on two different planes orthogonal to the z-axis. Both planes are separated by 100 mm. As we can see in Figure 3-1, the beams imaged have almost the same dimension, meaning that the beam is collimated.

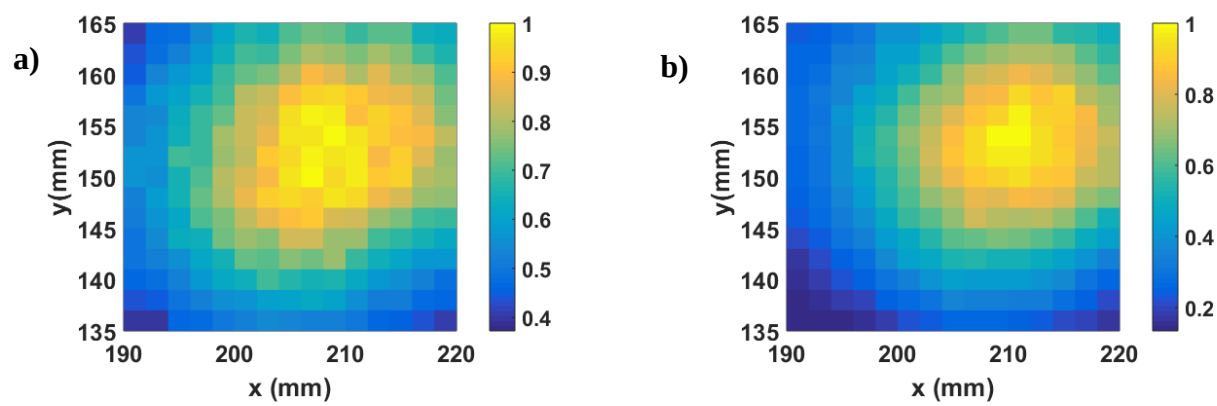

Figure 3-1: Distribution of the intensity of the pulse in different planes orthogonal to the z-axis. a) represents a plane at z=0 and b) represents a plane 100 mm farther from the transmitter.

When L2 is placed back in the setup, the detector is positioned at its focal point. The pulse recorded is presented in Figure 4-7 b and its associated spectrum is presented in Figure 4-7 c. As we can see, the pulse is very clearly defined and the spectrum is wide, with a bandwidth of around 1.5 THz.

3.3.2. Alignment of the system

To build a reflection-based time-resolved solid immersion microscope imaging a sample in the horizontal plane, the emitted THz pulse must be redressed vertically, be transmitted through a beam splitter, be focused on the sample, and have its reflection reflected on the beam splitter toward the detector. The proper functioning of the microscope requires a perfectly optimal alignment of these components, which would both assure the focusing of the beam to the diffraction limit and a minimization of the losses in the setup. A preliminary setup in which the focusing lens is not included is presented in Figure 4-8 a. In this setup, the pulse is reflected on a gold-coated mirror. It is intended to facilitate the alignment of the M1 mirror and the BS1 beam splitter. The detector is still on the 3D motorized stage to characterize the shape of the THz beam.

To consolidate the system and facilitate the alignment of M1 and BS1 at angles of 45°, a complete support is designed for 3D printing. This support additionally includes a system to position the SIL flat surface in the focal plane of the focusing lens. The full support (see Figure 4-9) is in four main parts. The parts fit into each other to form a rigid support protected against accidental shocks. The first two parts have cubic shapes and support M1 and BS1 (see Figure 4-12 c). The third part supports and centers the focusing lens on the beam. It also holds a system of printed racks and gears that enables the translation of the fourth part (which supports the SIL) along the vertical axis (see Figure 4-12 b).

From Figures 4-8 b and 4-8 c, it becomes obvious that the optical system affects the pulse significantly. The SNR of the pulse decreases sharply, its bandwidth is cut in half, and the double reflection on each side of the beam splitter introduces a pattern of interference in the spectrum.

3.3.3. Knife-edge experiment and resolution of the lenses

The last step in building the microscope consists in the addition of the L3 lens (see Figure 4-6) on the third part of the printed support. Considering a proper alignment of the system, this lens produced by Batop with a NA of 0.54 has a diffraction-limited spot size of 0.9259 λ. The choice of using a lens for focusing, although practical for this design of microscope, introduces chromatic aberrations in the system. The result is that the focal length of L3 varies slightly with the frequency. As we image with a pulse, the system will not be diffraction limited for the full bandwidth at the same position, and therefore the resolution needs to be measured at a specific frequency. With the intensity of the pulse being at its maximum around 0.1 THz, it is more practical to optimize the microscope at this frequency. To find the exact position of the focal length of L3 at 0.1 THz, multiple knife-edge experiments are executed at different distances from the lens (see Figure 4-10). For every position of the blade, the reflected pulse is recorded at the detector. For each pulse, the corresponding spectrum is calculated by Fourier transform. It is then possible to plot the specific intensity of each reflected pulse at 0.1 THz as a function of the position of the razor blade. When taking the intensity profile of 0.1 THz at different distances of the lens, the width of spot size (given by the FWHM of the first derivative of the profile, as explained in Section 1.1.2) decreases slowly until reaching a minimum and increasing again, as we can see in Table 3-1. The position of the minimal spot size is the position at which the resolution of the system is the best. The SIL can ultimately be added to the fourth part of the support, and its flat size is moved with the mechanism (see Figure 4-9 b) at the position identified.

Table 3-1: Spot size of the THz beam at 0.1 THz as a function of the distance of the lens.

Normalized distance from L3 [mm]	**Spot size [mm]**
0	2.84
0.5	2.64
1	2.53
2	2.30
2.5	2.87
3	3.31

This concludes the fabrication and characterization of the solid immersion microscope. In the next section, we present a submitted article where we explain in more detail the SILs' fabrication and their resolution measured on the microscope.

CHAPTER 4 ARTICLE 1: FABRICATION AND CHARACTERIZATION OF COMPOSITE TIO2-POLYPROPYLENE HIGH-REFRACTIVE-INDEX SOLID IMMERSION LENS FOR SUPER-RESOLUTION THZ IMAGING

4.1. Authors

Quentin Chapdelaine[1], Kathirvel Nallappan[1], Yang cao[1], Hichem Guerboukha[2], Nikita Chernomyrdin[3], Kirill Zaitsev[3] and Maksim Skorobogatiy[1]

1. *Polytechnique Montréal, 2500 Chemin de Polytechnique, Montréal, H3T 1J4, Canada*
2. *School of Engineering, Brown University, Providence, USA*
3. *Inst. of the Russian Academy of Sciences, Prokhorov General Physics Institute, Moscow, Russia*

Name of the journal: Optical Material Express

Submission date: April 22nd 2022

Publication date: TBD

4.2. Abstract

Terahertz (THz) near-field imaging is attracting a lot of attention for its potential applications in medical and material characterization. However, the spatial resolution of the recorded THz image was mainly limited by the diffraction limit of the commonly used lens in the THz microscopy system. Alternatively, a solid immersion lens (SIL) can be a promising approach for achieving super-resolution imaging as it reduces the spot size of the focused THz beam by a factor of 1/n, where 'n' is the refractive index (RI) of the lens material. In this work, we present the design and fabrication of hemispherical THz SIL using powder mixes of titanium dioxide (TiO_2) and polypropylene (PP) whose RIs are ~10 and ~1.51 at 1 THz, respectively, in the THz spectral range. In particular, we present two different lens fabrication strategies that are simple and cost-effective solutions. The first strategy uses pressing the TiO_2 powder with a PP powder at the Vicat temperature of PP while controlling the concentration of TiO_2 and the resultant lens porosity. The second design consists in pressing the TiO_2 powder in a hollow hemisphere that is 3D printed using PP. The fabricated lenses are then characterized physically and optically, and their RIs are

compared to the theoretical estimates using the Bruggeman model of the effective media. From the experimental measurements of the proposed SIL, a resolution limit as low as 0.20λ was achieved which is comparable to the best resolutions reported in the literature.

4.3. Introduction

In recent years, terahertz imaging has become one of the popular techniques in scientific and industrial applications mainly due to its non-invasive and high-resolution imaging capabilities when compared with infrared and microwave counterparts, respectively [46]. Due to the rapid development of high-power THz sources and efficient detectors, the commercial availability of THz imaging systems has become a reality. However, there are many challenges yet to be addressed before increasing its widespread applications in many areas. In THz imaging, one of the main challenges is the physical limitation in the resolution of THz waves which in free space is approximately ~0.5λ according to Abbe's diffraction limit [22]. For example, this limit implies that a THz pulse centered around 0.1 THz could not resolve features of the image smaller than 1.5 mm. This particular limitation hinders the application of THz imaging in several areas such as spectroscopy [47], medicine [51, 54], semi-conductor analysis [49], and security [55, 56]. Therefore, the development of a novel method to increase the spatial resolution of the THz imaging is the need of the hour.

Near-field (NF) imaging is one of the promising approaches which was developed to resolve the smallest features of the image [115]. Generally, in an NF imaging system, the information is collected within a few wavelengths of the sample, before the negative effects of diffraction degrade the image resolution [66, 116]. Solid immersion microscopy is an example of such a system. In this system, the focused incident beam propagates through a high refractive index hemispherical lens (or solid immersion lens (SIL)) located in the near-field of the sample. While propagating in this lens, the beam is confined by the dielectric response of the high RI medium. Behind the lens, the evanescent field still contributes to the beam's intensity, yielding a spot size smaller than the diffraction limit [117]. This system was first fabricated by Mansfield and Kino in 1990 when they reported the creation of a solid immersion microscope [6]. This microscope was initially applied to optical wavelengths which use a liquid with a refractive index of 2, which results in a slightly better resolution than air. Over time, the concept behind the solid immersion microscope was

rationalized, and the hemispherical SIL, whether liquid or solid, became a useful microscopy component in imaging laboratories [118]. In general, the spot size of a focused beam can be estimated using Equation1.

$$\delta = \frac{\lambda}{2\,NA} = \frac{\lambda}{2\,n\sin\theta} \qquad (4-1)$$

From Equation 1, δ is the spot size, λ is the free space wavelength of the beam, NA is the numerical aperture of the SIL, and θ is the half-angle of the cone of light focused by the lens. From Equation 1 it follows that the RI of the SIL plays a significant role in reducing the spot size and improving the resolution of the image.

In the THz regime, the availability of high RI material makes the solid immersion microscopy system a promising solution to achieve higher resolution. As reported in the literature, materials with RI above 3 give a significant improvement in the resolution of the THz imaging system [34]. The most widely used SILs, for example, are made of silicon whose RI in the THz range is approximately 3.5. This could be further improved by using the material having higher RI. By taking the advantage of longer wavelengths of the THz waves, many authors have reported metamaterials and metasurfaces with very high RI that will eventually be used in those systems [119, 120]. However, it could be more practical to simply use natural elements and more classical fabrication techniques to design the SILs. In this view, we aim at using TiO_2 in the fabrication of SIL as it has an RI of around 10 in the THz spectral range [112]. TiO_2 is a ceramic that is widely used in the industry, mainly because of its opacity which makes it a perfect white pigment[113, 121, 122]. It is generally produced as a powder by sintering, although it can as well be grown as a crystal in its most general form of rutile [123]. Moreover, it is commercially available in powder form and is rather inexpensive. As it is generally described as inert and not highly hazardous material, however, when used as a nanoparticle, it can also become an irritant and its inhalation can be dangerous. Nevertheless, the high RI property of TiO_2 can be of great interest in fabricating several THz components. For example, a SIL that is fabricated using pure TiO_2 could theoretically increase the resolution by a factor of 10. Therefore, the main objective of this work is to maximize the RI of the SIL by increasing the concentration of TiO_2.

So far, we have shown that TiO_2 could be an ideal material for the fabrication of a high RI solid immersion lens. However, a few fabrication challenges need to be addressed. TiO_2 is generally difficult to shape when it is in powder form and it requires high temperature (the sintering temperature of TiO_2 is between 400°C and 800°C), and high pressure (~ 1.5 GPa) [124, 125]. This requires very specific and expensive equipment for fabrication. TiO_2 can also be grown as a rutile crystal cylinder by epitaxial growth, and then be cut and polished in the shape of a hemisphere. This whole process, although providing a monocrystalline and ideally dense TiO_2 structure, would also prove itself extremely long and expensive [109]. Alternatively, shaping of TiO_2 structures using sol-gel techniques can be possible but demands specific equipment, and also it allows very limited concentration of TiO_2 which further results in lower RI of the SIL [107]. Therefore, a relatively simple and inexpensive technique must be identified for the fabrication of TiO_2 based THz SIL.

The paper is organized as follows. Firstly, we present two different approaches that we carried out in designing and optimizing the high-performance hemispherical SIL which is followed by the fabrication procedures. In both designs, we use PP as a secondary material to help shape the TiO_2 in a hemispherical form. Among all polymers, PP is chosen because of its reasonably high RI (measured at 1.510 for 1 THz) and low losses in the THz regime [91]. It is equally a resistant material whose low melting temperature (160°C) helps to shape and is already available in many forms for multiple applications. Secondly, we present the theoretical and experimental characterization of the proposed SILs. Since the lenses fabricated are composites of the two elements (TiO_2 and PP), their measured refractive index will be compared to the theoretical prediction of Bruggeman's model [126]. Finally, by carrying out the imaging experiment, we show that the resolution of the proposed SILs can be reduced to as low as 0.20λ at 0.09 THz which is well below Abbe's diffraction limit.

4.4. Design and Fabrication of hemispherical SIL

In this section, we present the two simple and repeatable design approaches that were carried out in the fabrication of SIL. The important parameters will be highlighted along with their limits and

appropriate design conditions. The TiO_2 powder was produced by Alfa Aesar in the rutile form, with a purity of 99.5% and particles size of 1-2 μm. Similarly, the PP powder used in this work was Propyltex 325S which was produced by Micro Powders, Inc. Its particle size is ~10-15 μm.

4.4.1. Fabrication of SILs using mechanical hot press (Pressed SIL)

The first design presents the pressing of a heated mix of TiO_2 and PP powders inside of a hemispherical mold. To help estimate the porosity once the SILs are fabricated, each mix is characterized by a weight concentration of TiO_2 (i.e., $m_{TiO_2}/(m_{TiO_2} + m_{PP})$, where m_{TiO_2} and m_{PP} are the mass of the TiO_2 and PP powders, respectively) and mix density (see Equation 2), where $\rho_{TiO_2} = 4.23$ g cm^{-3} and $\rho_{PP} = 1.07$ g cm^{-3} are the densities of TiO_2 and PP, respectively. In Table 1, we present the concentrations of TiO_2 and PP that were used in the fabrication of pressed SILs.

$$mix\ density = \frac{m_{TiO_2} + m_{PP}}{m_{TiO_2}/\rho_{TiO_2} + m_{PP}/\rho_{PP}} \qquad (4-2)$$

Table 4-1: Mass of TiO_2 and PP mixed to produce lenses of different concentration.

Mass PP [g]	**Mass TiO_2 [g]**	**Weight concentration of TiO_2**	**Mix density [g/cm^3]**
9.5165	56.4291	85.6%	2.9660
6.4965	59.5489	90.2%	3.2790
4.2711	67.7288	94.1%	3.5994

In what follows, we present the detailed fabrication procedure. The first step in the fabrication of the pressed lenses starts with the mixing of the powders. The homogeneity of the mix is critical to the successful fabrication of pressed SILs for two main reasons. Firstly, as PP will effectively act as glue (supporting matrix for TiO_2), it needs to be uniformly distributed within the mix to keep the TiO_2 particles in a solid structure. Secondly, one of the assumptions of any effective medium theory is that the inclusions composing the material are uniformly dispersed within the mix, thus, yielding a uniform effective RI. The PP and TiO_2 powders are therefore mixed in a high-energy ball mill for 30 minutes. A ball mill is a type of grinder (see Figure 1 a) consisting of a canister rotating at high speed in which the powders of interest are placed with hard ceramic balls [127].

As the canister rotates, the ceramic balls generate several high-speed collisions with the particles (see Figures 1 b and c), destroying the agglomerations and improving the homogeneity of the mix [128]. Additionally, the ball mill reduces the size of the particles due to collisions. This particle size reduction also helps minimize the gap between the PP particles (10-15 μm) and the TiO_2 particles (1-2 μm). Next, the powders are mixed again for 30 minutes with the V-1 Mini V Type Powder Mixer Machine (see Figure 1d). This machine uses the rotation of a V-shape canister to mix the powders and improve their homogeneity. During its rotation cycle, the powders are continuously gathered to the bottom of the canister before being separated equally on the two sides (see Figure 1 e and f). Considering the important difference of density in the two powders, this step significantly improves the mixing efficiency.

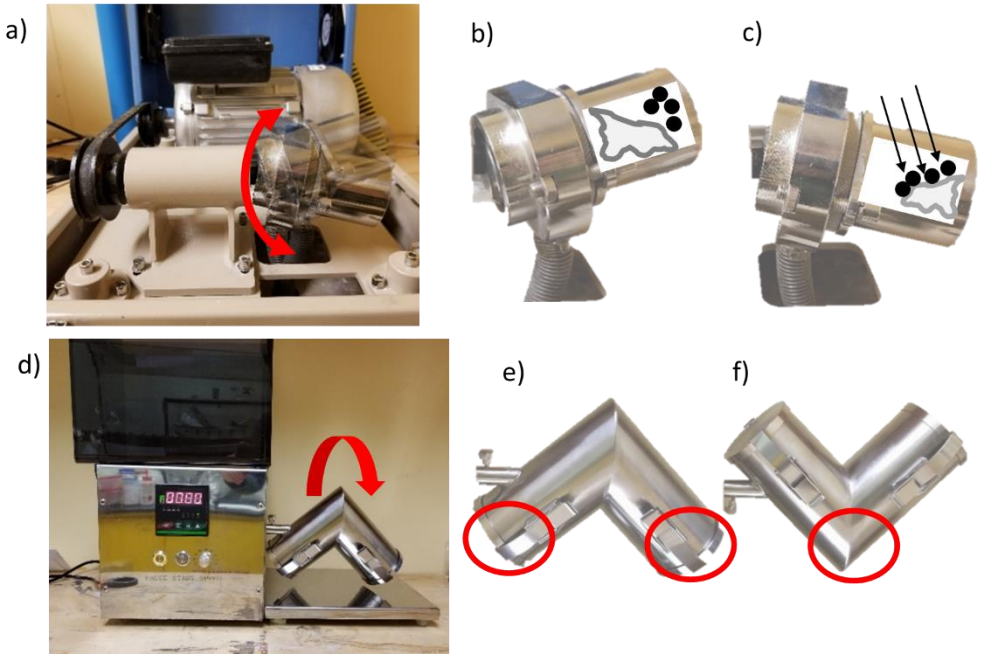

Figure 4-1: Photographs and schematics of the methods used to improve the homogeneity of the powder mix. a) Photograph of the high-energy ball mill used for the experiment. b) and c) Schematics of the working principle of the high-energy ball mill were the ceramic balls undergoes several collisions with the powders. The arrow marks represent the direction of the force. d) Photograph of the V-1 Mini V Type Powder Mixer Machine. The red arrow shows the direction of rotation. e) and f) Schematic of the working principle of the V-1 Mini machine. The red circles show the areas where the particles are gathered and separated.

In the second step, the mixed powders are transferred to the specially designed mold and pressed mechanically under heat. The mold consists of three main parts made of aluminum (see Figure 2

a). The bottom plates are drilled with a cylindrical hole on top of a hemispherical hole, both with a diameter of 25.4 mm (1 inch). An aluminum cylinder of the same dimensions as the cylindrical hole is used to apply pressure on the powder located inside of the hemispherical hole. The top plate was used to apply pressure evenly on the bottom two plates that contain the powder. The design of the mold with two bottom parts is intended to facilitate the removal of the SIL after the application of high pressure. Next, the hot press is heated to temperatures close to the Vicat temperature of PP (150°C) [94]. The Vicat softening temperature, in polymer science, describes a state in which the polymer softens and can be penetrated by other particles. The optimal temperature and pressure for mechanical stability of the resultant lenses are experimentally found at 135°C and 2 metric tons, respectively. It is noted that the mold was pressed for a total duration of 1 hour under this condition.

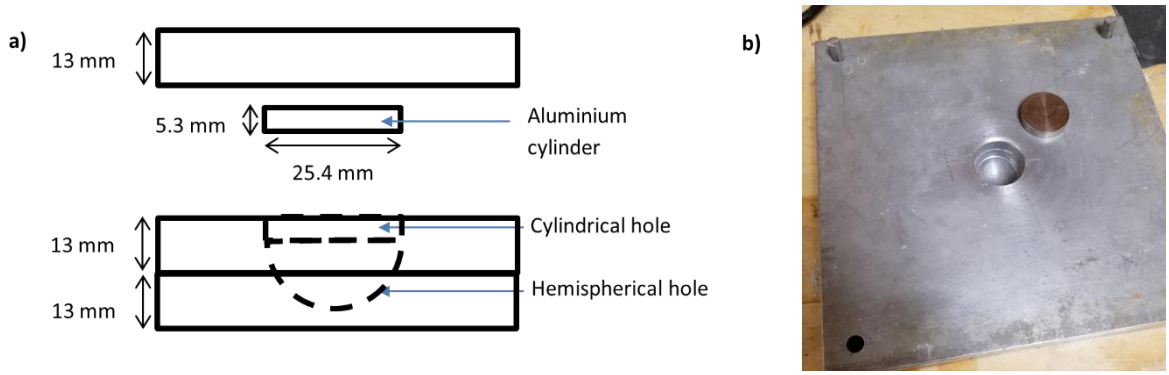

Figure 4-2: a) Dimensions of the mold in aluminum used to press the hemispherical SILs. b) Photograph of the mold.

Similarly, to estimate the RIs of the resultant SIL materials, a different mold shown in Figure 2 (a) was fabricated, where the hemispherical hole was replaced with the cylindrical geometry, while similar processing conditions and materials concentrations were used during sample fabrication (see Table 1). The shape of a cylinder sample makes it more practical to measure its RI and easier to press as the resultant samples are less fragile than a hemisphere. The cylinder RIs were then measured using THz spectroscopy and used as an approximation to the RIs of the pressed SILs. Particularly, two to four cylinders with a 25.4 mm diameter and 2 to 3 mm thickness are pressed for the same duration as the SIL while varying somewhat the porosity for every mix (see Table 2) by changing the amount of the material in the mold. Next, the mold was left to cool down to room temperature. Then, the cylinders and hemispheres are carefully taken out of the molds and polished

with sandpaper of 120, 400, and 1000 grits [129]. Their mass and dimensions after polishing the samples are measured. The volume of the air inclusion (f_{air}) can be estimated by comparing the density of the sample (m_{sample}/V_{sample}) to the powder mix density calculated in Table 1. In the case of an ideally dense lens, there would be no air inclusion, and the density of the sample would be the same as the density of the powders. The air inclusion (or porosity) is however unavoidable due to the limitations of the press and of the mold (aluminum is a rather soft metal that cannot sustain very high pressure). The porosity is estimated using Equation 3, while the derivation of this equation is given in the appendix:

$$f_{air} = 1 - \frac{sample\ density}{mix\ density} \qquad (4-3)$$

In what follows, the term porosity means the air filling factor by volume calculated by Equation 3. This expression of porosity gives the filling factor of air inside of the structure from which it is possible to estimate the theoretical effective RI of the SIL using, for example, the Bruggeman model. It is observed during the experiments that the lowest achievable porosity also depends on the concentration of TiO_2. This is because the deformation capacity of the PP allows it to better fill the pores when it is in higher concentration. Thus, using higher concentrations of TiO_2 (which leads to higher RI of the samples), generally results in higher sample porosities, and in samples that are more fragile and tend to break during removal from the mold. At 94.1% TiO_2, the lowest porosity achieved at which a lens is still mechanically stable is 41 %. A slightly lower porosity is achieved in the cylindrical samples for a similar concentration. The properties of the fabricated cylinders and SILs are presented in Table 2 and Table 3, respectively.

The volume filling factor of the TiO_2 and PP inclusions in each sample can be calculated simply through their mass in the 3 powder mixes and their density. Dividing the mass by the density gives the volume of each inclusion. The ratio

$$f_{TiO_2} = \left(\frac{m_{TiO_2}/\rho_{TiO_2}}{m_{TiO_2}/\rho_{TiO_2} + m_{PP}/\rho_{PP}}\right) \cdot (1 - f_{air}) \qquad (4-4)$$

$$f_{PP} = 1 - f_{air} - f_{TiO_2} \qquad (4-5)$$

Table 4-2: Composition of the sets of cylinders fabricated to characterize the refractive index of samples built with the press.

wt. % TiO_2	Mix density [g cm^{-3}]	Volume [cm^3]	Mass [g]	Density [g cm^{-3}]	Porosity	Set porosity
85.6%	2.966	1.40	2.618	1.87	36.9%	38.5%
		1.43	2.601	1.82	38.6%	
		1.50	2.677	1.78	40.0%	
		1.58	3.117	1.97	33.5%	30.7%
		1.49	3.054	2.04	31.1%	
		1.47	3.007	2.04	31.2%	
		1.53	3.182	2.08	29.9%	
		1.50	3.076	2.04	31.1%	29.0%
		1.53	3.316	2.17	27.0%	
		1.57	3.110	1.98	33.2%	
		1.64	3.226	1.97	33.5%	
90.2%	3.278	1.62	3.311	2.05	37.5%	37.5%
		1.63	3.330	2.05	37.5%	
		1.52	3.247	2.14	34.6%	34.8%
		1.44	3.080	2.13	34.9%	
		1.46	3.225	2.21	32.6%	33.2%
		1.44	3.133	2.17	33.8%	
94.1%	3.599	1.30	3.017	2.32	35.6%	35.9%
		1.35	3.082	2.29	36.5%	
		1.37	3.176	2.32	35.5%	

Table 4-3: Properties of the pressed SILs fabricated

% TiO_2	Mix density [g cm^{-3}]	Volume [cm^3]	Mass [g]	Sample density [g cm^{-3}]	Porosity
85.6 %	2.966	4.29	9.050	2.11	28.9%
90.2 %	3.279	4.29	10.120	2.36	28.1%
94.1%	3.599	4.29	9.085	2.12	41.2%

In Figure 3, we show the fabricated SILs that are removed from the mold structure. Polishing must be carried out to improve the surface quality. It is noted that the grey stains on the 85.6% TiO_2 and 90.2% TiO_2 SILs are due to silicon oil used in the mold to simplify lens release.

Figure 4-3: Photographs of the top and bottom surface of the pressed SILs. From left to right, the SIL with 94.1% TiO_2, 90.2% TiO_2 and 85.6% TiO_2.

4.4.2. The printed SIL

The second design is intended to create a SIL made of pure TiO_2 powders (without PP inclusions). A thin hemispherical shell was 3D printed (Raise3D pro2) using PP filament inside which the TiO_2 powders are pressed manually. The thickness of the shell is 1.5 mm, with PP deposited using a 50 µm-thick layers and a 200 µm diameter nozzle. The high 3D printing precision is necessary to minimize the surface roughness of the hemispherical shell and reduce the diffraction of the THz beam (see Figure 4).

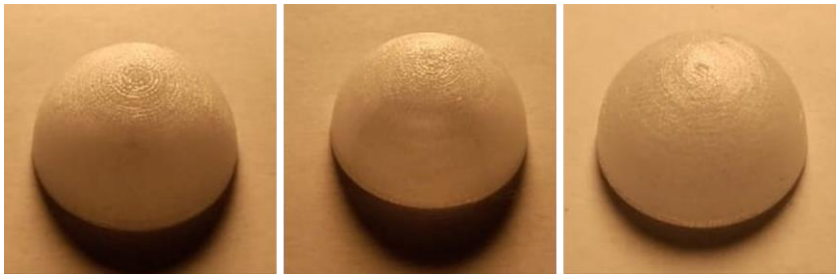

Figure 4-4: Comparison of the thin hemispherical shells of PP that are 3D printed with layer heights of 100 µm, 80 µm and 30 µm (from left to right).

The quality of the surface roughness of the 3D printed shell is an important element of this SIL design. The thickness of 1.5 mm is particularly chosen so that the shell is solid enough for the TiO_2 powder to be compressed inside of it while being thin enough to minimize the shell absorption losses. It is noted that 3D printing with PP is challenging as it is very sensitive to temperature gradients which affects strongly the model adherence to the build plate. To improve adherence of the 3D printed sample to the build plate, the plate temperature was set to 95°C. The filament extrusion temperature was set at 240°C. The extrusion speed is 15 mm/s.

Next, the 3D printed hemispherical shell was filled with pure TiO_2 powder, and manually pressed to avoid the breakage of the shell (see Figure 5 (a-e)). The porosity of the SIL fabricated using this approach can be estimated using Equations 3 and 4, thus resulting in $f_{air} = 52.7\%$ and $f_{TiO_2} = 47.3\%$, which is the highest fraction of TiO_2 among all the fabricated lenses.

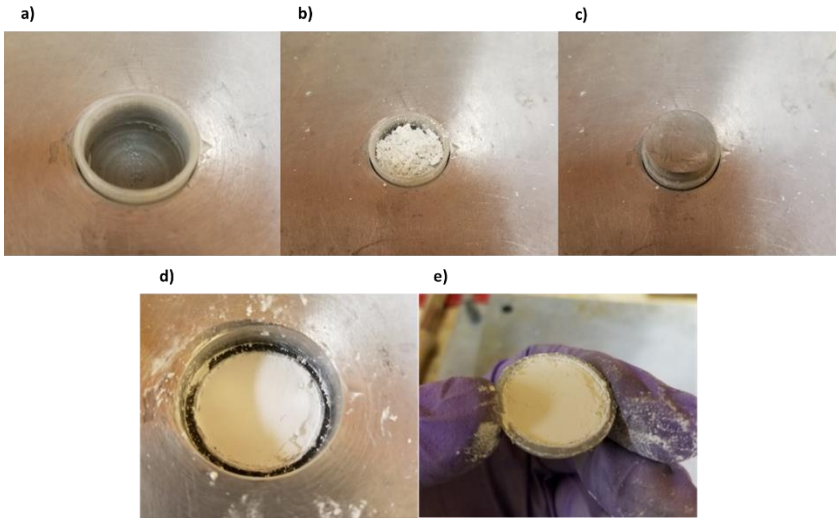

Figure 4-5: Photographs showing the step by step process by which the SILs are fabricated using the pure TiO_2 powder in a 3D printed shell. (a)The 3D printed hemispherical shell was placed on the hemispherical aluminum mold (b). The pure TiO_2 powders are filled inside the 3D printed shell. (c) Aluminum cylinder that helps in manually pressing the TiO_2 powder (d). The printed SIL after pressing it manually (e). The 3D printed hemispherical with filled TiO_2 powder was removed carefully from the mold.

4.5. Resolution of the SILs

In this section, we describe the optical characterization of the fabricated SILs. The resolution of the fabricated SILs is characterized using the THz time-domain-spectroscopy (TDS) system [21, 36, 37, 45]. The schematics of the experimental setup are shown in Figure 6. A high-power femtosecond laser (Mai Tai) with an average power of ~2.5 Watts and a wavelength of 800 nm was used as the optical source to drive the emitter and detector photoconductive antennas (PCA). The THz emitter is an interdigital array antenna fabricated by Batop Optoelectronics (iPCA-21-05-1000-800-h). The antenna array was mounted with a hemispherical silicon lens and a TPX lens in the same housing to produce an almost collimated beam. A secondary TPX lens (L1) with a focal length of 151.5 mm is added and positioned experimentally to collimate the beam.

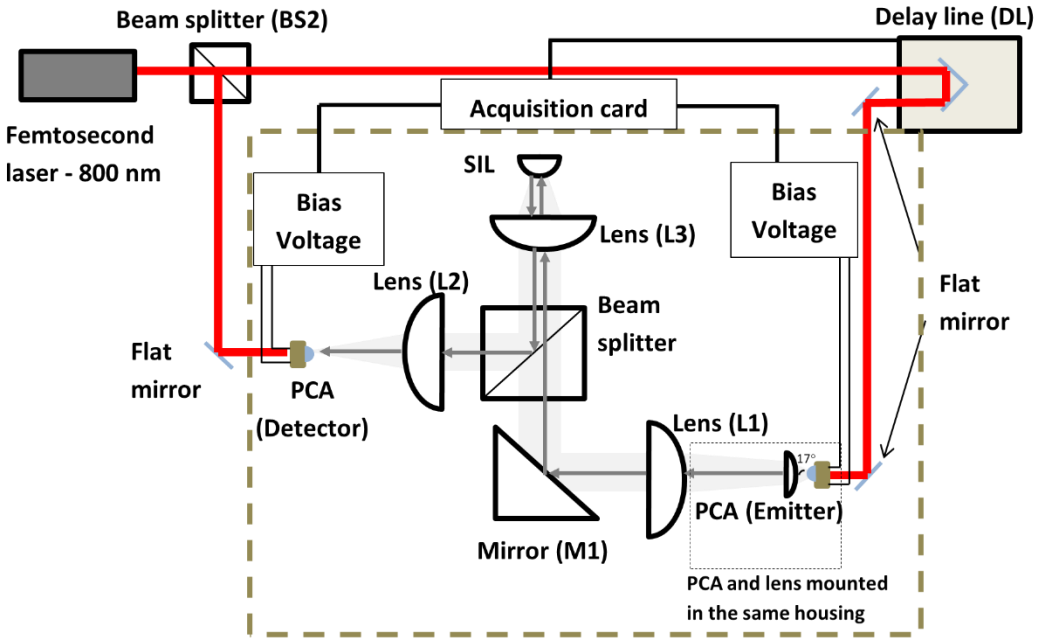

Figure 4-6: Schematic of the pulsed THz imaging system with SIL.

The collimated beam from the lens L1 is then deviated vertically by a flat gold-coated circular mirror with a diameter of 50mm (M1) so that the sample (which should be located on top of the SIL), can be scanned in the horizontal plane while illuminated from the bottom. The THz beam passes through the beam splitter BS1 for the first time before L3, and a second time after being reflected on the sample. A thin silicon wafer of thickness ~200 μm was used as the beam splitter (BS1). Similarly, L3 is a TPX THz lens from Batop optoelectronics with a diameter of 50 mm and

a focal length of 35 mm whose NA is 0.54. The theoretical spot size of lens L3 is estimated as 0.9259 λ. The THz lenses L1 and L2 are identical and are fabricated using PTFE with a focal length of 151.5 mm and a diameter of 2 inches. The detector is a PCA manufactured by Menlo (TERA8-1). It is noted that the spot size of the SIL was measured in the NF of the flat surface.

To characterize the THz beam produced by the emitter PCA, a first experiment was conducted by focusing the collimated beam directly on the detector PCA (see Figure 7 (a)). For this arrangement, we present the time-resolved THz pulse (see Figure 7 (b) and its corresponding Fourier transform with a bandwidth of ~1.5 THz (Figure 7 (c)).

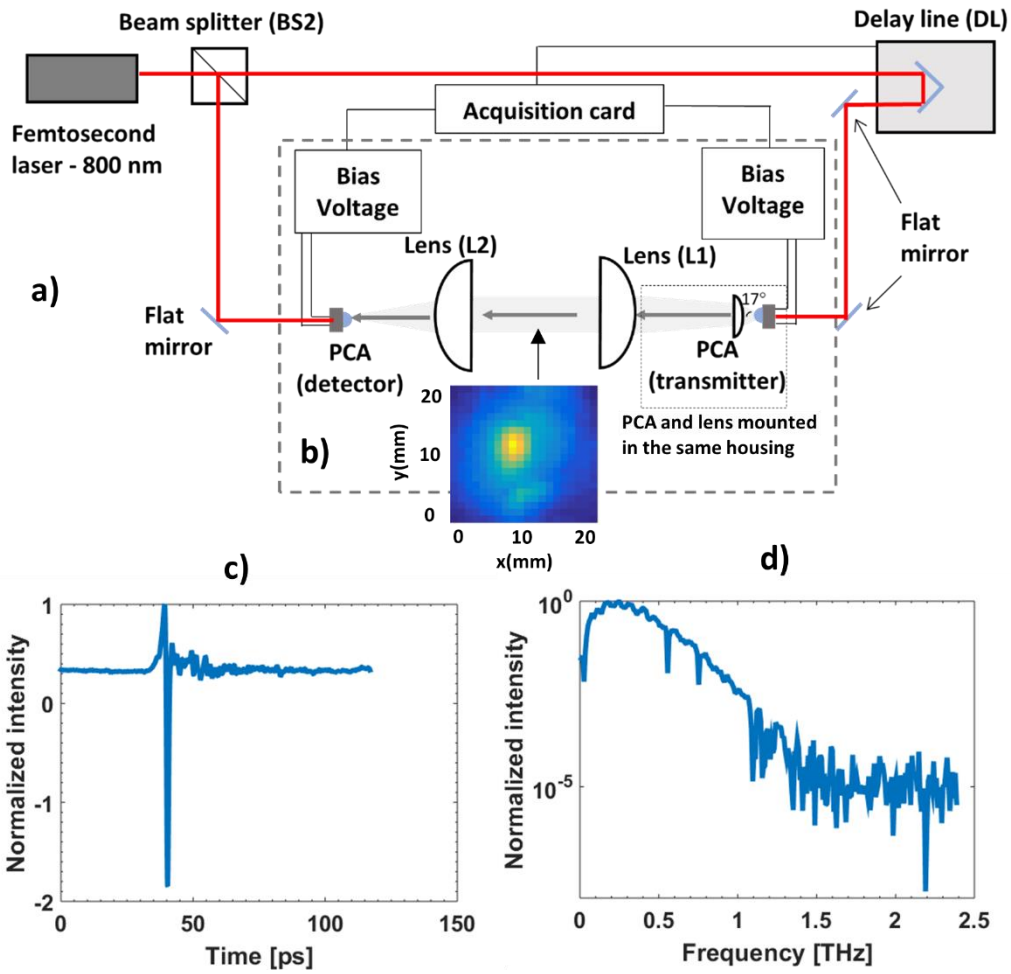

Figure 4-7: a) Schematic of the experimental set up to measure the spot size of the lens, L1. (b) 3D plot of the intensity of the electromagnetic field in the propagation plane of the pulse (the plot represents a 20mm x 20mm square). (c) The normalized intensity distribution of the time-domain THz pulse recorded after L1 and d) the corresponding Fourier transform of the pulse in frequency domain.

A second experiment was conducted with a simplified version of the THz solid immersion lens system as shown in Figure 8 (a). Here, support is 3D printed in 4 parts to help align the optical component of the microscope (see Figure 9). A reference spectrum (without SIL) was measured by using a mirror to redirect the beam towards the detector. In Figures 8 (b) and 8 (c), the THz time-domain pulse recorded with this setup is presented which highlights the impact of the imaging system on the THz pulse. i.e. The THz beam intensity was decreased significantly as it passes through the beam splitter (BS1). We also note the effect of interference patterns in the Fourier transform of the time-domain pulse (see Figure 8 (c)), due to the internal reflection on each face of the beam splitter. Finally, by comparing the spectral width shown for the empty system (see Figure 7 (c)) (1.5 THz), we observe that the spectral width for the experimental setup shown in Figure 8 (a) reduces significantly to ~0.7 THz.

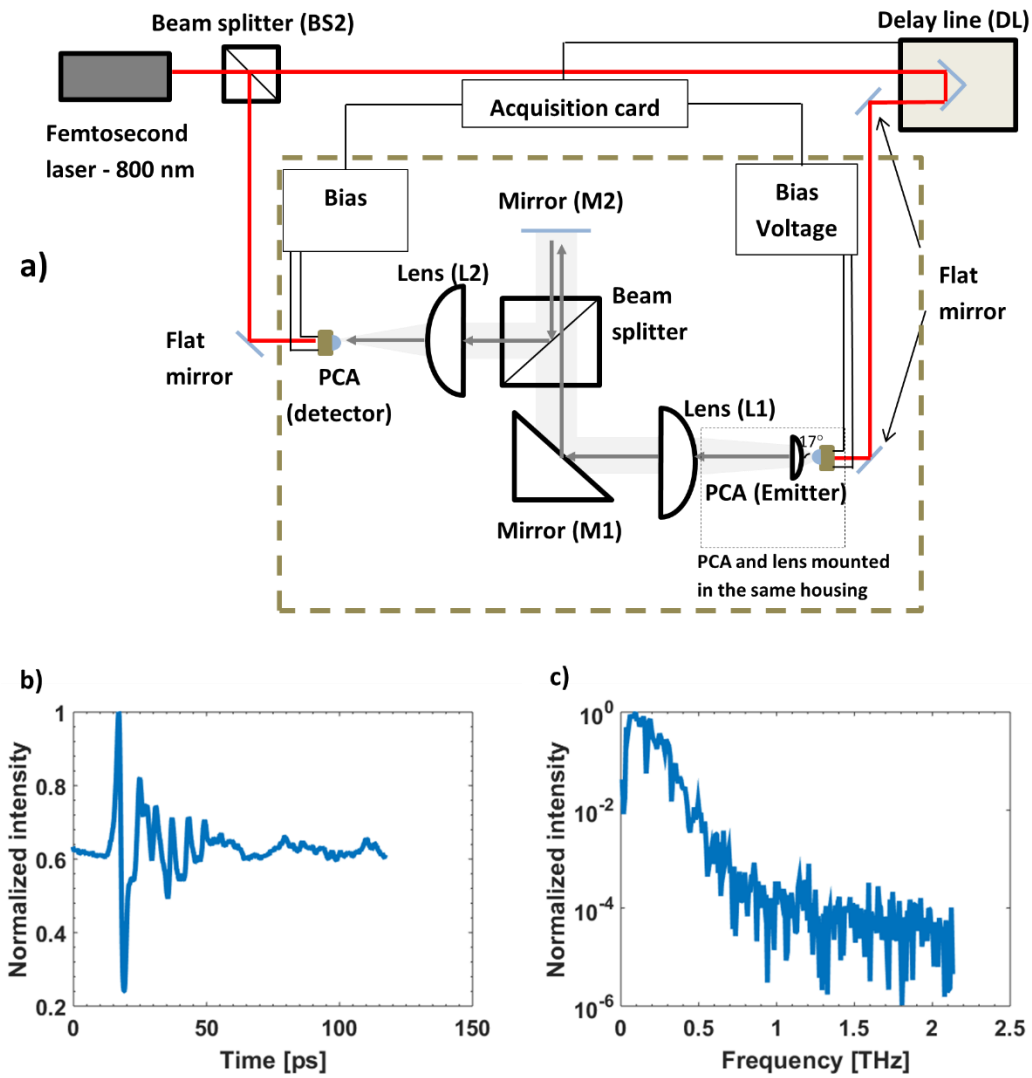

Figure 4-8: a) Schematic of the experimental setup of the THz imaging system to characterize the SIL. (b) The normalized intensity distribution of the time-domain THz pulse and c) the corresponding Fourier transform of the pulse in frequency domain.

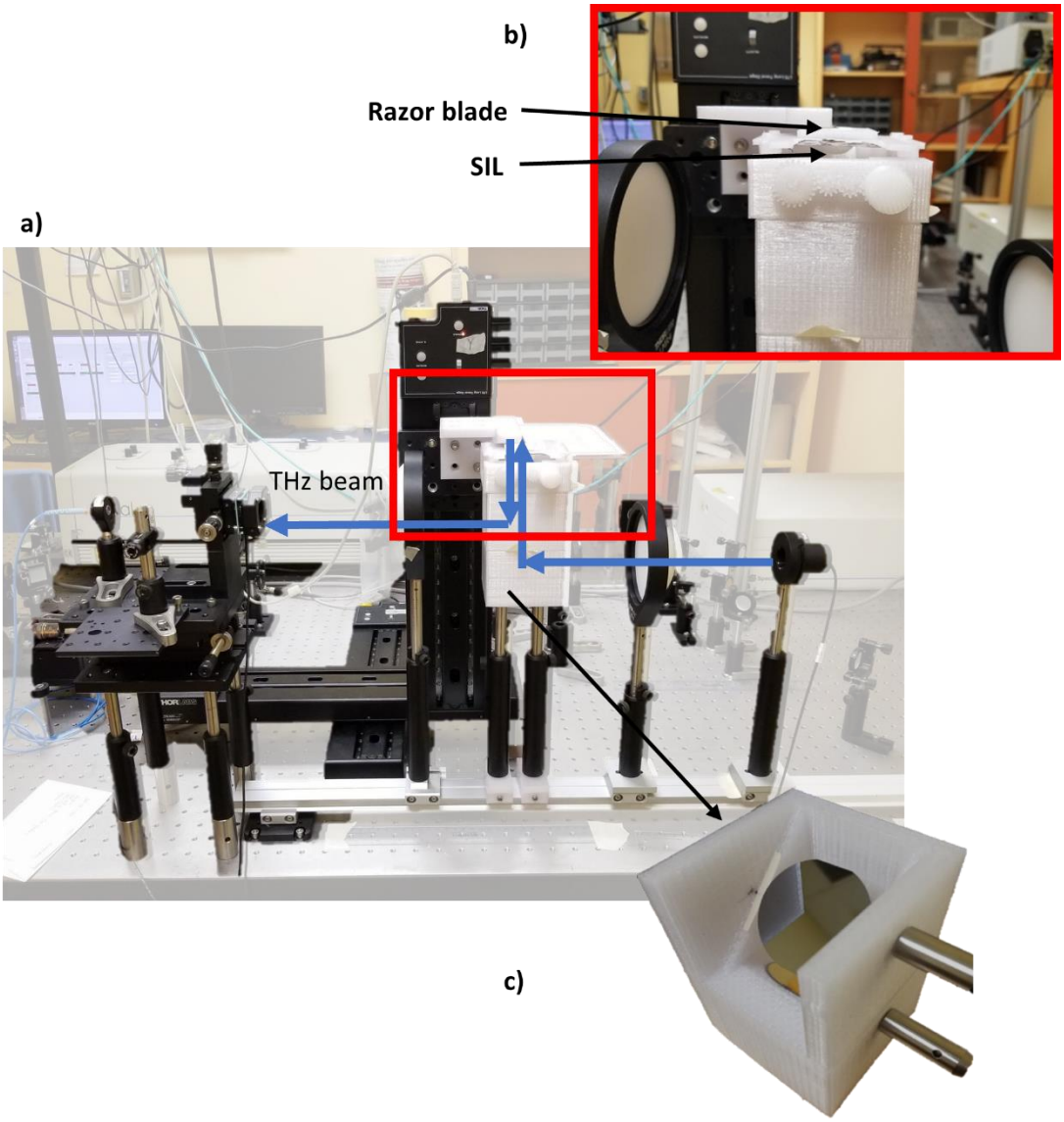

Figure 4-9: a) Schematics of the 4-parts support 3D printed for the fabrication of the solid immersion system. b) Photographs of the first two parts printed and with the M1 and BS1 inserted. c) Photographs of the complete system in the configuration of a knife-edge experiment.

Despite the notable loss in the spectral width (~0.7 THz) of the detected THz beam, it is still sufficient enough to carry out the THz imaging experiments. It demonstrates that the 3D printed support provides the necessary alignment for the microscope. The complete solid immersion system of Figure 6 is therefore ultimately built.

A knife-edge experiment was carried out to perform the following measurements: the spot size produced by Lens 3 without SIL, the spot sizes with the pressed SILs of 85.6%, 90.2%, and 94.1%

TiO_2 (see Table 3), and the spot size with the printed SIL (described in Section 3.2). Due to the chromatic aberration of L3, the focal plane will not be the same for all frequencies carried by the pulse. To take advantage of the higher power generated by the PCA at 0.1 THz, the system is aligned to image the beam at the focal point of that frequency. The measure of the profile is made by a knife-edge experiment. The measurement entails moving a razor blade in the focal plane of L3 (which coincides with the flat side of the SIL when present) and recording the reflected intensity with a spatial resolution much smaller than the beam spot size. As the edge of the razor blade moves toward the center of the beam, the reflected intensity will increase and define the intensity profile of the beam. The first-order derivative of this profile yields a gaussian-like function representing the increase in reflected intensity as a function of the axial coordinate of the beam. The resolution of the system is defined by the full width at half maximum (FWHM) of the Gaussian beam profile (see Figure 10) [7].

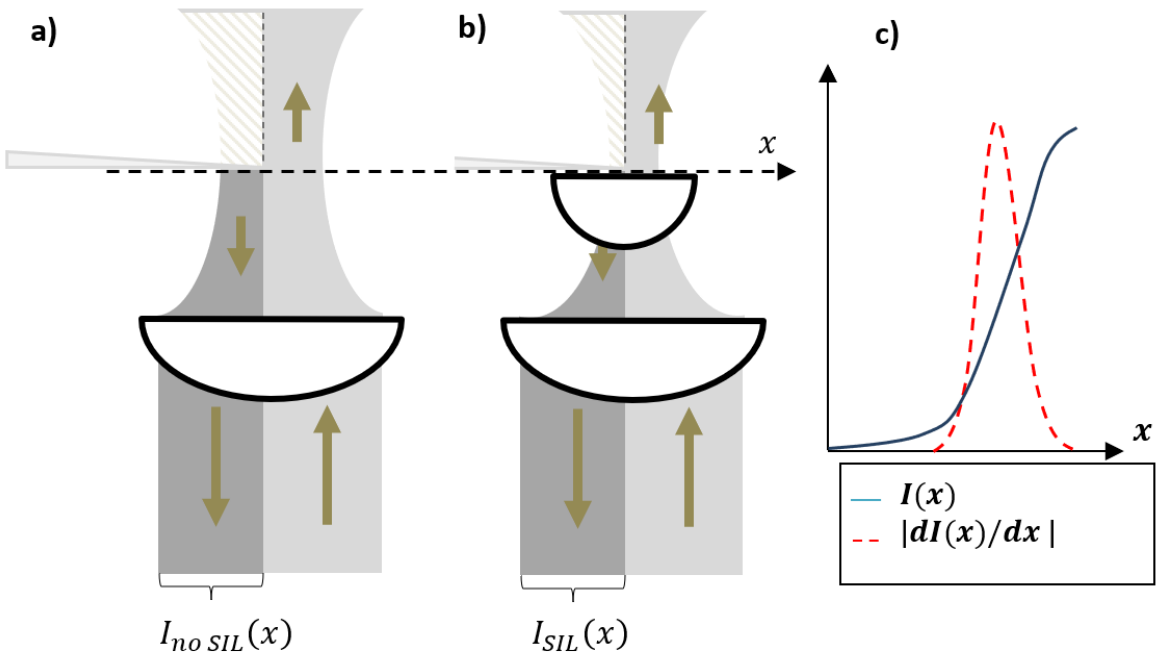

Figure 4-10: Schematic of a reflection-mode knife-edge measurement technique to measure the resolution of the THz imaging system. a) Scenario without SIL. b) Scenario with a SIL, which reduces the spot size. c) Representation of the intensity profile drawn when plotting the intensity of the pulse recorded as a function of the knife edge position.

To characterize the SILs, the displacement step of the knife-edge is set between 10 and 25 µm. At every step, between 65 and 100 pulses are recorded and averaged. Each pulse corresponds to 1753 measures of the electric field taken by an acquisition card at 2500 Hz with a delay line moving at 25 mm s^{-1}, giving a scan duration of approximately 120 ps. The measured profile is smoothed by a simple moving average algorithm, and the derivative of the smoothed curve is drawn.

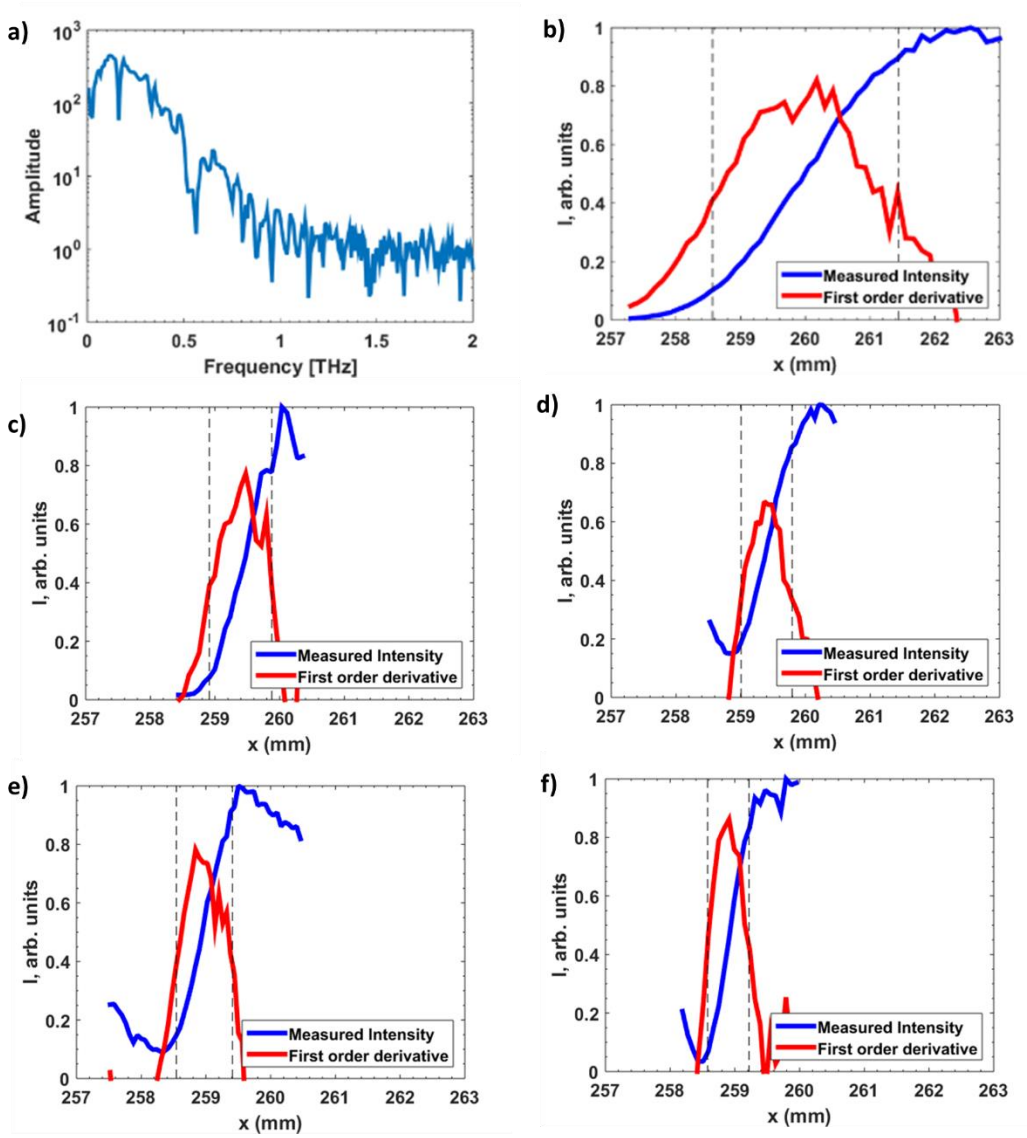

Figure 4-11: Characterization of the SILs using knife-edge experiments. The blue curve represents the normalized intensity (I) profile of the reflected THz pulse at 94 GHz and the red curves represent the first order derivative of the intensity. a) Frequency domain spectrum of the THz pulse detected by the system without any SIL. b) System without SIL, c) SIL with 85.6% TiO_2 d) SIL with 90.2 % TiO_2, e) SIL with 94.1% TiO_2 and f) Printed SIL.

As shown in Figure 11, the spot size of the bean focused by L3 at 0.094 THz is 3.189 mm, or 0.90 λ. This beam size corresponds to the diffraction limit of the system and will serve as a reference for the SILs. The same experiment is made for each of the SILs. In Table 4, we present the beam width at 0.094 THz for different SILs discussed in this work. The distance between each fitted point on the intensity profile obtained by knife edge is between 60 and 125 μm, depending on the lens tested. This gives a profiles whose precision is smaller than 4% of the wavelength, yielding an estimation of the precision of the resolution measurement.

Table 4-4: Resolution of the solid immersion system at 0.094 THz for the fabricated SILs.

f **(THz)**	**No SIL**	**SIL 85.6%**	**SIL 90.2%**	**SIL 94.1%**	**Printed SIL**
0.094	0.90 λ	0.30 λ	0.24 λ	0.27 λ	0.20 λ
Experimental RI		3.00	3.75	3.33	4.50

The experimental RI presented in Table 4 corresponds to the improvement of resolution due to the SIL presence ($RI = spot\ size_{without\ SIL}\ /\ spot\ size_{with\ SIL}$), as follows from Equation 1. We can see from Figure 11 that the presence of SIL dramatically increases the system resolution. Moreover, 0.20 λ resolution achieved using a printed PP shell with compactified TiO_2 powder SIL competes with the highest resolution of 0.15 λ reported in the literature that uses high resistivity Si [7].

4.6. Characterization of the RI of SILs fabricated using mechanical hot press technique

To validate the experimentally found RIs from Table 4, the Bruggeman model is used to theoretically predict RIs of the lenses using the air, PP, and TiO_2 filling factors presented in Table 3. To give more context to the validity of the Bruggeman model, we refine our analysis by also taking direct measures of the RI of the pressed cylinders while using a standard cutback technique. The cylinder filling factors are presented in Table 3. In Figure 12 (a), we present a schematic of

the experimental setup, while details of the THz CW spectroscopy system operation can be found in References [114, 130]. Briefly, the setup consists of two distributed feedback lasers operating with slightly different center wavelengths in the infrared C-band. The output of each laser is fiber-coupled and the two are combined and equally split using a 3dB coupler. After passing through the piezoelectric fiber stretcher, the laser beams optically drive the emitter and detector photomixer. The THz waves are then generated from the emitter photomixer by applying the modulating bias voltage. By using a pair of parabolic mirrors, the generated THz beam is collimated and focused on to the detector photomixer for lock-in detection. The cylindrical samples are placed in the collimated THz beam path and the complex RI of the sample is measured using the cutback technique. The resultant findings for the cylinder RIs sare summarized in Figures 12 b, 12 c and 13. The cutback technique is a very precise and convenient non-destructive way to measure directly the complex RI of a sample.

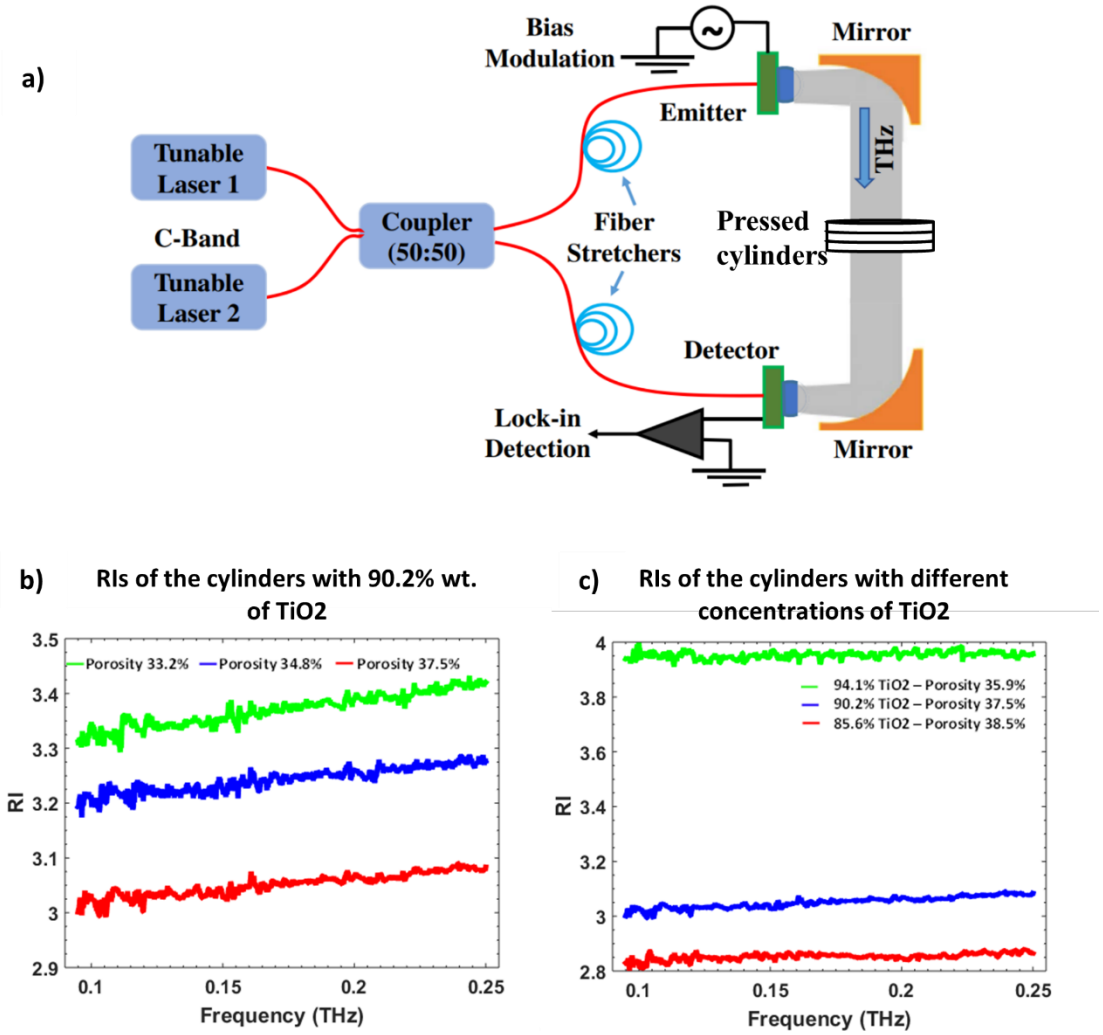

Figure 4-12: a) Schematic of the CW THz spectroscopy system b) RIs of the cylinders with 90.2% wt. of TiO_2 for different porosities and (c) RIs of the cylinders with different concentrations of TiO_2.

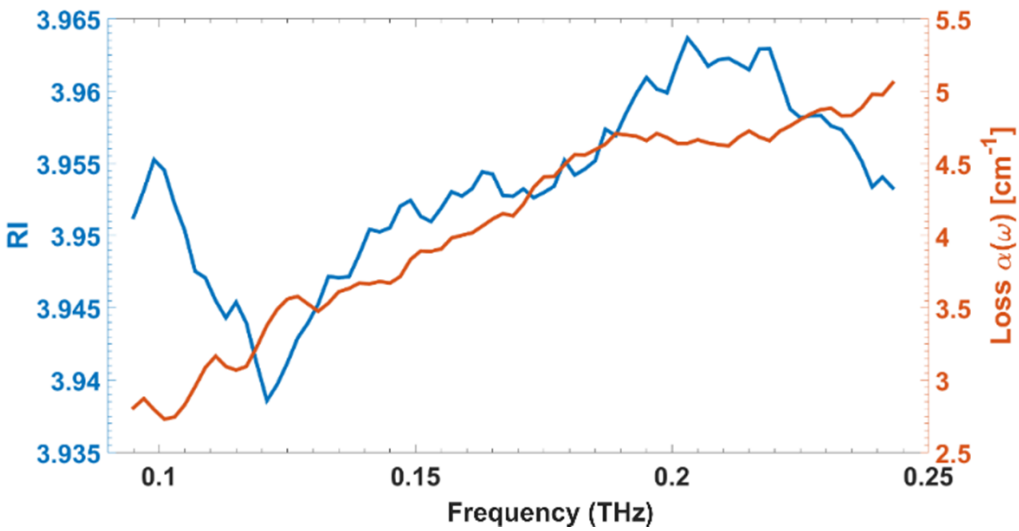

Figure 4-13: Refractive index and losses by field of the cylinder with 94.1 wt. % TiO_2 for a porosity of 35.9%.

The plots presented in Figures 12 (b) and (c) confirm that the RI increases for higher values of the TiO_2 volume filling factor (f_{TiO_2}). In Figure 12 (b), we observe that as porosity (f_{air}) increases, the RI decreases. In Figure 12 (c), we see that at similar values of f_{air}, the RI increases with the increasing concentration of TiO_2. At 94.1% of TiO_2 (see Figure 13), the least porous cylinder pressed had a porosity of 36% (the least porous SIL had a porosity of 41%) and a RI around 3.95 at 0.1 THz. In the same plot (Figure 13), we present the absorption loss (by field) of a particular cylindrical sample that corresponds to a pressed SIL with the highest RI.

Next, assuming that the shape of the particle is spherical, the effective RI (n_{eff}) is approximated by using the Bruggeman model by solving Equation 6:

$$f_{air}\frac{n_{air}-n_{eff}}{n_{air}+2\cdot n_{eff}}+f_{TiO_2}\frac{n_{TiO_2}-n_{eff}}{n_{TiO_2}+2\cdot n_{eff}}+f_{PP}\frac{n_{PP}-n_{eff}}{n_{PP}+2\cdot n_{eff}}=0 \qquad (4-6)$$

where, f_{air}, f_{TiO_2} and f_{PP} are the volume fraction of air, TiO_2, and PP, respectively (their summation must be equal to 1). Similarly, n_{air}, n_{TiO_2}, and n_{PP} are the RIs of air, TiO_2, and PP, which are 1, 10 [131], and 1.51, respectively at ~0.1 THz.

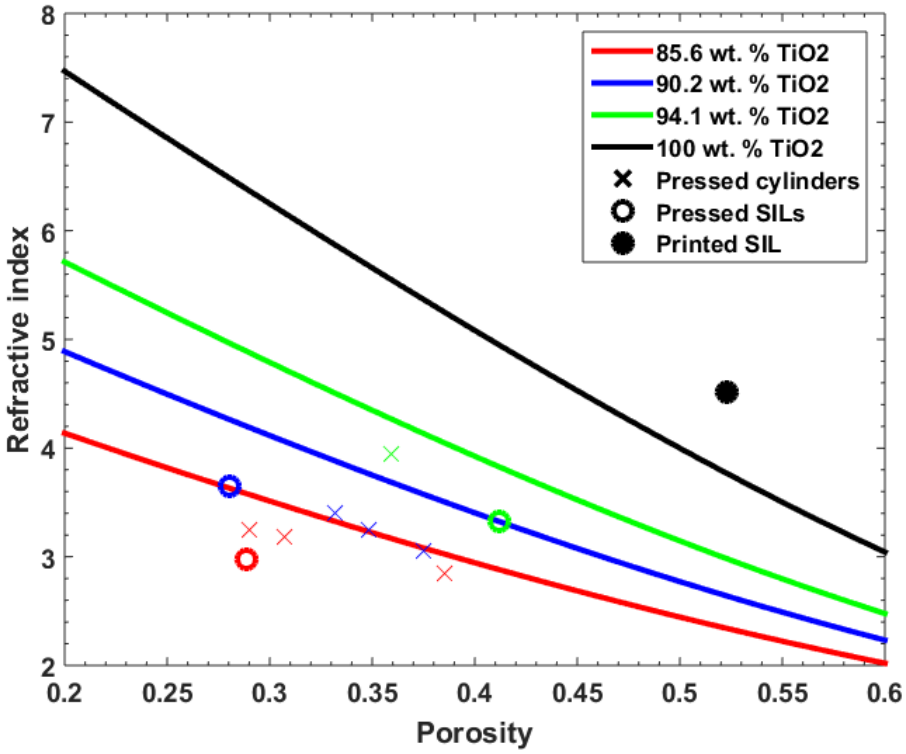

Figure 4-14: Theoretical prediction using Bruggeman model for estimating the effective RI of the SILs.

In Figure 14, as continuous curves, we present the theoretical estimates of RIs for the pressed powder mixes of different concentrations of TiO_2. On the same graph using the "x" and "o" markers, we present experimentally measured values of the RIs for cylinders and SILs, respectively at 0.1 THz. The color of the lines and markers represent different concentrations of the TiO_2 in the TiO_2/PP powder mixes, namely red - 85.6 wt. % TiO_2, blue - 90.2 wt.% TiO_2, green - 94.1 wt.% TiO_2, and black - 100 wt.% TiO_2. Only a qualitative agreement between the experimental and experimental data is observed. This finding is not surprising as Bruggeman model is known to work well only in the limiting cases of very low or very high values of the filling factors, while for the intermediate values of the filling factors one can only hope for a qualitative agreement.

4.7. Conclusion

In conclusion, this paper reported on the fabrication of SILs based on two design strategies (mechanical hot press technique of TiO_2/PP mixes, and 3D printed SIL shell with TiO_2 powder compactification), that could be used to enhance the resolution of THz imaging well beyond the Abbe's diffraction limit. The fabricated SILs are characterized and tested using a pulsed SIL THz microscope system. The improvement in resolution is quantified using the knife-edge measurements of the beam waist after focusing with and without SIL. The best resolution of 0.2 λ at 0.1 THz is achieved using a 3D printed SIL shell with compacted pure TiO_2 powder, while the second-best resolution of 0.25λ is achieved using a pressed TiO_2/PP SIL with 90.2 wt. % TiO_2 concentration. Both results compete well with the highest resolution of 0.15 λ reported today in a THz SIL system that uses expensive high resistivity Si materials.

4.8. Disclosures

The authors declare no conflict of interest. Q. Chapdelaine conducted process development for the pressed and 2D printed SIL fabrication, assembled the SIL microscopy system, performed materials characterization, and wrote the paper. K. Nallapan, Y. Cao, and H. Guerboukha have developed the original pulsed and CW imaging and spectroscopy systems and helped adapt them to conduct material characterization and SIL microscopy reported in this paper. N. Chernomyrdin and K. Zaitsev have advised on the layout and design of the pulsed SIL imaging system, provided some of the custom optics for the system, and contributed to the paper writing. Finally, M. Skorobogatiy was the author of the idea, supervised the project, and contributed to writing the paper.

4.9. Appendix

Here we show derivation behind Equation 3 that allows experimental measurement of porosity of the pressed samples using the weights of the TiO_2 and PP powders in the mix, as well as the total volume of a sample.

$$Porosity = air\ filling\ factor\ by\ volume$$

$$= \frac{V_{air}}{V_{total}}$$

$$= 1 - \frac{V_{TiO2} + V_{PP}}{V_{total}}$$

$$= 1 - \frac{m_{TiO2}/\rho_{TiO2} + m_{PP}/\rho_{PP}}{V_{total}}$$

$$= 1 - \frac{\frac{m_{TiO2}}{\rho_{TiO2}} + \frac{m_{PP}}{\rho_{PP}}}{V_{total}} \cdot \frac{m_{total}}{m_{total}}$$

$$= 1 - \frac{\left(\frac{m_{TiO2}}{\rho_{TiO2}} + \frac{m_{PP}}{\rho_{PP}}\right)/m_{total}}{V_{total}/m_{total}}$$

$$= 1 - \frac{m_{total}/V_{total}}{m_{total}/\left(\frac{m_{TiO2}}{\rho_{TiO2}} + \frac{m_{PP}}{\rho_{PP}}\right)}$$

$$= 1 - \frac{m_{total}/V_{total}}{(m_{TiO2} + m\_PP)/\left(\frac{m_{TiO2}}{\rho_{TiO2}} + \frac{m_{PP}}{\rho_{PP}}\right)}$$

m_{total}/V_{total} is the density of the cylinder lense measured experimentally after fabrication

$(m_{TiO2} + m\_PP)/\left(\frac{m_{TiO2}}{\rho_{TiO2}} + \frac{m_{PP}}{\rho_{PP}}\right)$ is the mix density defined in Equation 2.

CHAPTER 5 GENERAL DISCUSSION

In this chapter, we will discuss how well our results answer our original objectives. We will also present possible improvements to the project, and discuss certain parameters that can be changed in the experimental part.

In summary, the main objective of the project was to fabricate SILs using TiO_2 powder and a simple fabrication method that would achieve super-resolution. More specifically, we were interested in exploring the resolution improvement of a system that would use TiO_2 lenses rather than Si lenses. Whereas the latter is very well covered in the literature (see Table 2-2), very few authors covered applications with the former. Furthermore, Si lenses are very expensive for a limited improvement of resolution. The focus was therefore set on designs that could yield a RI higher than 3.5 while being cost-efficient. Both designs finally chosen only differ by the presence of a third inclusion in the lens for the pressed SIL. From a practical point of view, the first design (the pressed SIL) was more useful for manipulation since the fabricated lens was solid and could either be used in both a horizontal or a vertical microscope. The second design sacrificed some of this practicality to reach a higher RI. However, it was more fragile and necessitated a vertical microscope. As this lens ended up being the best one (its resolution at 0.20044 λ is among the best in the literature), it does fit our initial objective. Our results however do not perfectly fit the expected RI predicted by the Bruggeman model. Although an important reason, as was discussed in our article in **Chapter 3**, is that our experimental evaluation of the volume of the SILs has a very large margin of error, a few factors could be changed to improve the method.

5.1. Porosity

The first factor, porosity, is the main factor that prevents us from reaching the full potential of TiO_2. In Figure 4-14, we see that a SIL with a weight percentage of 94.1% TiO_2 would reach a RI of 4.0 when its porosity is at 39%. Unfortunately, we were never able to press a lens at this concentration with a porosity lower than 40%. To the best of our knowledge, the failure to do so is due to two factors: the hot press pressure was not high enough and the particles were too big. As a

matter of fact, the pressure of two metric tons applied by the press was limited by the fragility of the mold. At the start of the project, the mold (see Figure 4-2) was designed as reported in reference [92]. For fabrication purposes, the material was chosen to be plates of aluminum. Considering the pressure necessary to press ceramic powders, it would have been better to use a harder metal, such as steel. When applying higher pressures, the aluminum mold would deform, which limited the density achievable. A different mold would allow higher pressure which could yield lower porosity. With a more robust mold and a more sophisticated press, we could even achieve sintering temperature and pressures as reported in Section 1.4.2, which would yield an even higher RI. This could yield some of the best THz SILs reported in the literature. Another way to improve the density achievable would be to reduce the particle size. The TiO_2 particles being initially much smaller than the PP particles (1-2 μm and 10-15μm), it was determined that using a high-energy ball mill would help to break the agglomerations within the mix, crush the particles, and reduce the difference in size. The longer the powder spends in the high-energy ball mill, the more the particle size will be reduced. An idea to consider would be to significantly increase the time in the ball mill from 30 minutes (time of ball milling for the SILs fabricated in this project) to a few hours, to have particles much smaller than one micron. With smaller particles, higher density would be achievable, and porosity could theoretically be decreased much more.

5.2. Absorption

One of the main issues faced in this project is a general one in THz science, which is the limited power generated by sources. As a source, this project uses a Batop interdigital array antenna which generates a very powerful pulse of light compared to more conventional PCAs (up to 100 mW according to the datasheet). However, some problems with our laser (the Mai Tai from Spectra physics) prevented us from reaching the maximal power with the PCA. Furthermore, our reflection-mode solid immersion system makes the pulse travel twice through a beam splitter, dividing its intensity by 4. Then, travelling through 50 mm of TiO_2 lens would make the detected pulse extremely weak. In Figure 5-1, we compare the normalized intensity of the pulses recorded without a SIL to the ones recorded with the two SILs with the highest RI (the pressed SIL with 90.2% TiO_2 and the printed SIL). The detected pulses attenuated by the fabricated SIL have roughly 20% of the

intensity of the initial pulse. It is obvious that although the SILs were designed to minimize absorption, the losses are very important. The pulses plotted in Figure 5-1 are an average of 100 pulses measured at the detector. Such a large number of pulses is necessary to improve the SNR of the system but is also very time-consuming.

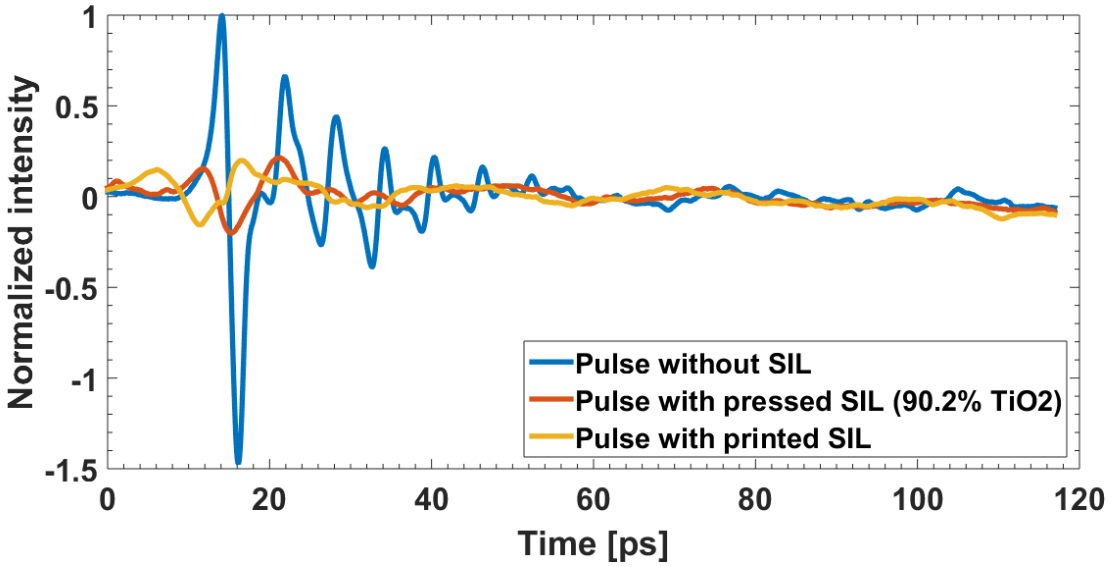

Figure 5-1: Comparison of the intensity of the pulses having traveled through a SIL and the intensity of the initial pulse.

An idea to improve the intensity of the detected THz would be, intuitively, to use a more powerful THz source. Indeed, a BWO could generate a higher output of monochromatic THz waves, which, especially because of the chromatic aberrations in this system, would be much more efficient. However, it does not change the reality that BWOs are rare and very expensive. Another idea would be to reduce the diameter of the SIL, from 25.4 mm to about 10 mm for example. It would require many modifications in the microscope (collimating the beam to a shorter radius, changing the focusing lens, etc) and in the fabrication process (changing the mold, reducing the layer height of the 3D printer to keep a smooth surface, etc), but it would considerably reduce the losses of the system, making it much more practical for actual applications. Considering that absorption follows Beer-Lambert law and that losses decrease exponentially with the distance traveled by light in a given medium, reducing this distance by half would greatly improve the SNR of the detected pulse.

5.3. Surface roughness

Another source of errors in the system was the surface of the fabricated SIL. The experiments being at the frequency of 0.1 THz (i.e., a wavelength of approximately 3 mm), imperfections at the surface of the SIL are not as important as in the visible or IR range. It remains important, however, to achieve a good polishing of the SILs' flat side in order to have good results with the knife-edge experiments. However, the polishing of the spherical face is more difficult. In this project, the pressed SILs' spherical surfaces were polished superficially with sandpaper sheets of 120, 400, and 1000 grits to remove as many obvious flaws as possible. Working at higher frequencies in the THz range would require a more thorough polishing, which would affect the spherical shape of the SIL. Using a tool adapted to polish optical lenses in the visible would be necessary to extend the applicable range of frequency of the fabricated SIL.

5.4. Chromatic aberrations

The last aspect to be discussed about the project is the choice to design a time-resolved pulsed microscope with lenses. This choice, which introduces the chromatic aberration, limits the upside of a pulsed microscope because the resolution becomes frequency-dependent. In this project, the microscope schematic of Figure 4-6 was mainly adopted because of practical considerations and because of its simplicity (which matched the time limitations of the project). It was a simple setup that met the basic requirements, which were to measure the resolution of the fabricated SILs while illuminating them with a vertical beam. A more optimised system would rely on a parabolic mirror to provide a focus without aberrations (see Figure 5-2). Another upgrade could come from the use of a beamsplitter cube rather than the Si slab used for this project. The reason we used the current beam splitter is that the THz has a wide diameter (approximately 40 mm) and that no beamsplitter cubes of that size were available at the time when the components were ordered. In the eventuality that such a part became available, it would remove the noticeable interference pattern on the pulses (see the secondary pulse in Figure 5-1). This improvement is not a necessity for the functioning of the microscope but would be an upgrade.

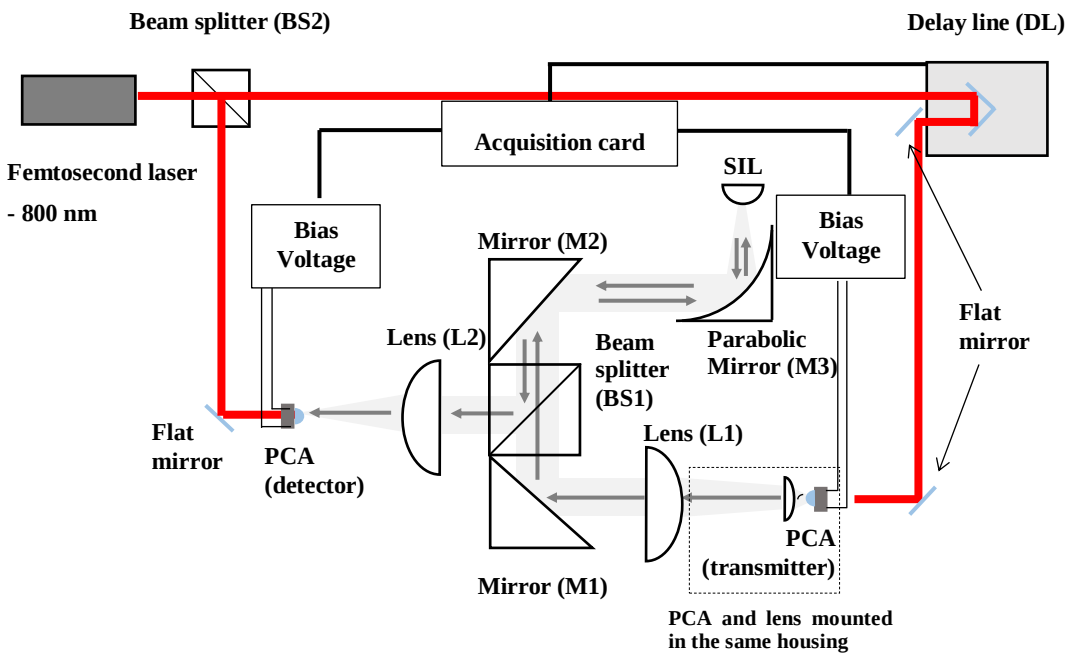

Figure 5-2: Proposition of an adapted solid immersion microscope in which the beam is focused with a parabolic mirror instead of a lens.

CHAPTER 6 CONCLUSION

In conclusion, this thesis presented the fabrication of SILs in TiO_2 following two designs. The SILs are hemispherical lenses used in a solid immersion microscope to achieve super-resolution in THz imaging. Super-resolution (i.e., resolution beyond the diffraction limit) is necessary for many THz imaging potential applications. The high RI of TiO_2 (approximately 10) makes this material very interesting for SIL fabrication, as it provides a potential for better resolution than the Si SILs which are used in most recent publications.

First, we proposed our fabrication methods for the two designs. These methods are easy to implement and use a TiO_2 powder that is widely available. The first method simply consists in pressing the TiO_2 powder with PP powder in a hemispherical mold at 135°C. The second method consists in pressing pure TiO_2 powder inside of a 3D printed PP hemispherical shell. The objective is to maximize the concentration and density of TiO_2 in the SILs in order to optimize the resolution. The Bruggeman model is used to estimate the RI of the four SILs fabricated.

The RI of cylinders fabricated with the same method as the pressed SILs is measured by the cutback technique. The estimation made with the Bruggeman model overestimates the measures by a significant margin (around 10%), but the demonstration is made that the SILs fabricated have a RI close to or higher than the Si SIL. The measurements also show that the RI of the SILs depends mainly on two parameters: the concentration of TiO_2 and the porosity in the SIL. Control over these parameters gives control over the RI, which can then be used to optimize the fabricated lenses.

A complete and functional reflection-based time-resolved solid immersion microscope is built and characterized. The THz pulse is produced by a PCA and has a bandwidth of 0 to 1.5 THz with a maximum intensity around 0.1 THz. The system reduces this bandwidth from 0 to approximately 0.7 THz. The spot size of the beam focused through the fabricated SILs is measured by the knife-edge technique and super-resolution is demonstrated.

In our submitted paper, we presented in detail the fabrication method and resolution of the SIL. The SILs fabricated are characterized and the solid immersion microscope built is presented. The final resolution of the best SILs is measured at 0.20047 λ, which compares very well to the best system reported in the literature.

Finally, the results are discussed. The SILs provide a resolution improvement factor that shows a lot of potential for applications in the literature. Ideas to further increase the RI of the SILs are proposed based on the literature review. Improvements in the fabrication methods are also presented as consideration for future research. The solid immersion microscope is functional, but improvements are proposed to make it more practical for applications in THz imaging.

REFERENCES

[1] Safian, R., G. Ghazi, and N. Mohammadian, *Review of photomixing continuous-wave terahertz systems and current application trends in terahertz domain*. Optical Engineering, 2019. **58**(11): p. 110901 (28 pp.).

[2] Tarekegne, A.T., et al. *THz-induced ultrafast modulation of NIR refractive index of silicon. in 2016 41st International Conference on Infrared, Millimeter, and Terahertz waves (IRMMW-THz)*. 2016.

[3] Minin, O., et al., *Improvement of a point-contact detector performance using the terajet effect initiated by photonics*. Optical Engineering, 2020. **60**(8): p. 082005.

[4] Hillger, P., et al., *Terahertz Imaging and Sensing Applications With Silicon-Based Technologies*. IEEE Transactions on Terahertz Science and Technology, 2019. **9**(1): p. 1-19.

[5] D'Arco, A., et al., *THz Pulsed Imaging in Biomedical Applications*. Condensed Matter, 2020. **5**(2): p. 25.

[6] Mansfield, S.M. and G. Kino, *Solid immersion microscope*. Applied physics letters, 1990. **57**(24): p. 2615-2616.

[7] Chernomyrdin, N.V., et al., *Reflection-mode continuous-wave 0.15 λ-resolution terahertz solid immersion microscopy of soft biological tissues*. Applied physics letters, 2018. **113**(11): p. 111102.

[8] Masters, B.R., *Ernst Abbe and the Foundation of Scientific Microscopes*. Optics and Photonics News, 2007. **18**(2): p. 18-23.

[9] Stelzer, E.H.K., *Beyond the diffraction limit*. Nature Photonics, 2009. **3**(7): p. 361-361.

[10] Saleh, B. and M. Teich, *Fundamentals of Photonics*, 2nd Edition. 2nd ed. Wiley Series in Pure and Applied Optics, ed. B.E.A. Saleh. 2009, Hoboken, New Jersey, USA: John Wiley & Sons. 1177.

[11] Pedrotti, F.L., L.S. Pedrotti, and L.M. Pedrotti, *Introduction to Optics* (3rd edition). 3rd ed, ed. E. Fahlgren. 2007: Pearson education.

[12] Mugnai, D., A. Ranfagni, and R. Ruggeri, *Pupils with super-resolution*. Physics Letters A, 2003. **311**(2): p. 77-81.

[13] Di Francia, G.T., *Super-gain antennas and optical resolving power*. Il Nuovo Cimento (1943-1954), 1952. **9**(3): p. 426-438.

[14] Grosjean, C.C., *Note on the diffraction of light by a finite number of centres distributed at random*. Il Nuovo Cimento (1943-1954), 1952. **9**(3): p. 220-234.

[15] Dyba, M. and S. Hell, *Focal Spots of Size λ / 23 Open Up Far-Field Florescence Microscopy at 33 nm Axial Resolution*. Physical review letters, 2002. 88: p. 163901.

[16] Bollanti, S., P. Di Lazzaro, and D. Murra, *How many times is a laser beam diffraction-limited?* Optics Communications, 1997. **134**(1): p. 503-513.

[17] Orlov, S., et al., *Toward a Corrected Knife-Edge-Based Reconstruction of Tightly Focused Higher Order Beams*. Frontiers in Physics, 2020. **8**(572).

[18] de Araújo, M.A., et al., *Measurement of Gaussian laser beam radius using the knife-edge technique: improvement on data analysis*. Applied Optics, 2009. **48**(2): p. 393-396.

[19] Roggenbuck, A., et al., *Coherent broadband continuous-wave terahertz spectroscopy on solid-state samples*. New Journal of Physics, 2010. **12**(4): p. 043017 (13 pp.).

[20] Lewis, R.A., *A review of terahertz sources*. Journal of Physics D: Applied Physics, 2014. **47**(37): p. 374001.

[21] Reimann, K., *Table-top sources of ultrashort THz pulses*. Reports on Progress in Physics, 2007. **70**(10): p. 1597-1632.

[22] Guerboukha, H., K. Nallappan, and M. Skorobogatiy, *Toward real-time terahertz imaging*. Advances in Optics and Photonics, 2018. **10**(4): p. 843-938.

[23] Consolino, L., S. Bartalini, and P. De Natale, *Terahertz Frequency Metrology for Spectroscopic Applications: a Review*. Journal of Infrared, Millimeter, and Terahertz Waves, 2017. **38**(11): p. 1289-1315.

[24] Chevalier, P., et al., *Widely tunable compact terahertz gas lasers*. Science, 2019. **366**(6467): p. 856-860.

[25] Paiella, R., et al., *Self-Mode-Locking of Quantum Cascade Lasers with Giant Ultrafast Optical Nonlinearities*. Science, 2000. **290**(5497): p. 1739-1742.

[26] Raab, J., et al., *Ultrafast two-dimensional field spectroscopy of terahertz intersubband saturable absorbers*. Optics Express, 2019. **27**(3): p. 2248-2257.

[27] Lobanov, Y., et al., *Time-resolved measurements of light–current characteristic and mode competition in pulsed THz quantum cascade laser*. Optical Engineering, 2021. **60**(8): p. 082019.

[28] Asada, M., S. Suzuki, and N. Kishimoto, *Resonant Tunneling Diodes for Sub-Terahertz and Terahertz Oscillators*. Japanese Journal of Applied Physics, 2008. **47**(6): p. 4375-4384.

[29] Sengupta, K., T. Nagatsuma, and D.M. Mittleman, *Terahertz integrated electronic and hybrid electronic–photonic systems*. Nature Electronics, 2018. **1**(12): p. 622-635.

[30] Rieh, J., D. Yoon, and J. Yun. *An overview of solid-state electronic sources and detectors for Terahertz imaging*. in 2014 12th IEEE International Conference on Solid-State and Integrated Circuit Technology (ICSICT). 2014.

[31] Booske, J.H., et al., *Vacuum Electronic High Power Terahertz Sources*. IEEE Transactions on Terahertz Science and Technology, 2011. **1**(1): p. 54-75.

[32] Dobroiu, A., et al., *Terahertz imaging system based on a backward-wave oscillator*. Applied Optics, 2004. **43**(30): p. 5637-5646.

[33] Garcia Jomaso, A., et al. *Continuous wave microscopy based on solid immersion lens*. in 2019 44th International Conference on Infrared, Millimeter, and Terahertz Waves (IRMMW-THz), 1-6 Sept. 2019. 2019. Piscataway, NJ, USA: IEEE.

[34] Chernomyrdin, N.V., et al., *Solid immersion terahertz imaging with sub-wavelength resolution*. Applied Physics Letters, 2017. **110**(22).

[35] Auston, D.H., *Picosecond optoelectronic switching and gating in silicon*. Applied Physics Letters, 1975. **26**(3): p. 101-103.

[36] Auston, D.H., K.P. Cheung, and P.R. Smith, *Picosecond photoconducting Hertzian dipoles*. Applied Physics Letters, 1984. **45**(3): p. 284-286.

[37] Burford, N. and M. El-Shenawee, *Review of terahertz photoconductive antenna technology*. Optical Engineering, 2017. **56**(1): p. 010901.

[38] Kolner, B. and D. Bloom, *Electrooptic sampling in GaAs integrated circuits*. IEEE Journal of Quantum Electronics, 1986. **22**(1): p. 79-93.

[39] Glazov, M.M. and S.D. Ganichev, *High frequency electric field induced nonlinear effects in graphene*. Physics Reports, 2014. **535**(3): p. 101-138.

[40] Wu, Q. and X.C. Zhang, *Free-space electro-optic sampling of terahertz beams*. Applied Physics Letters, 1995. **67**(24): p. 3523-3525.

[41] Wu, Q., T.D. Hewitt, and X.C. Zhang, *Two-dimensional electro-optic imaging of THz beams*. Applied Physics Letters, 1996. **69**(8): p. 1026-1028.

[42] Xie, X., J. Dai, and X.C. Zhang, *Coherent Control of THz Wave Generation in Ambient Air*. Physical Review Letters, 2006. **96**(7): p. 075005.

[43] Katyba, G.M., et al., *THz generation by two-color laser air plasma coupled to antiresonance hollow-core sapphire waveguides: THz-wave delivery and angular distribution management*. Optics Express, 2022. **30**(3): p. 4215-4230.

[44] Zhou, B.B., Q. Shen, and P.U. Jepsen. *Wavelength dependence of high-energy air-plasma THz generation under optimal conditions*. in 2020 45th International Conference on Infrared, Millimeter, and Terahertz Waves (IRMMW-THz). 2020.

[45] Hu, B.B. and M.C. Nuss, *Imaging with terahertz waves*. Optics Letters, 1995. **20**(16): p. 1716-1718.

[46] Mittleman, D.M., *Twenty years of terahertz imaging [Invited]*. Optics Express, 2018. **26**(8): p. 9417-9431.

[47] Takahashi, M., et al., *Intermolecular hydrogen bond stretching vibrations observed in terahertz spectra of crystalline vitamins*. CrystEngComm, 2018. **20**(14): p. 1960-1969.

[48] van Exter, M., C. Fattinger, and D. Grischkowsky, *Terahertz time-domain spectroscopy of water vapor*. Optics Letters, 1989. **14**(20): p. 1128-1130.

[49] Joyce, H.J., et al., *A review of the electrical properties of semiconductor nanowires: insights gained from terahertz conductivity spectroscopy*. Semiconductor Science and Technology, 2016. **31**(10): p. 103003.

[50] Komandin, G., et al., *Dielectric permittivity of organosilicate glass thin films on a sapphire substrate determined using time-domain THz and Fourier IR spectroscopy*. Journal of Physics D: Applied Physics, 2021.

[51] Musina, G.R., et al., *Prospects of terahertz technology in diagnosis of human brain tumors – A review*. 2020, 2020. **6**(2).

[52] Zotov, A., et al., *In situ terahertz monitoring of an ice ball formation during tissue cryosurgery: a feasibility test*. Journal of Biomedical Optics, 2021. **26**(4): p. 043003.

[53] Musina, G.R., et al., *Optical Properties of Hyperosmotic Agents for Immersion Clearing of Tissues in Terahertz Spectroscopy*. Optics and Spectroscopy, 2020. **128**(7): p. 1026-1035.

[54] Kucheryavenko, A.S., et al., *Terahertz dielectric spectroscopy and solid immersion microscopy of ex vivo glioma model 101.8: brain tissue heterogeneity*. Biomedical Optics Express, 2021. **12**(8): p. 5272-5289.

[55] Murrill, S.R., et al., *Terahertz imaging system performance model for concealed-weapon identification*. Applied Optics, 2008. **47**(9): p. 1286-1297.

[56] Liu, H.B., et al., *Terahertz Spectroscopy and Imaging for Defense and Security Applications*. Proceedings of the IEEE, 2007. **95**(8): p. 1514-1527.

[57] Rahman, A., et al., *THz spectroscopic sensing of liquid chemicals using a photonic crystal fiber*. OSA Continuum, 2020. **3**(11): p. 2982-2996.

[58] Ebensperger, T., et al. *Influences on 3D image quality in a high-resolution Xray laminography system*. 2014. IOP Publishing Ltd.

[59] Jr., R.E.F., G.M. Decad, and S.R. Hetzler, *Volumetric density trends (TB/in.3) for storage components: TAPE, hard disk drives, NAND, and Blu-ray*. Journal of Applied Physics, 2015. **117**(17): p. 17E301.

[60] Hell, S.W., *Far-Field Optical Nanoscopy*. Science, 2007. **316**(5828): p. 1153-1158.

[61] Jeong, D. and D. Kim, *Super-resolution fluorescence microscopy-based single-molecule spectroscopy*. 2022.

[62] So, P.T.C., et al., *Two-Photon Excitation Fluorescence Microscopy*. Annual Review of Biomedical Engineering, 2000. **2**(1): p. 399-429.

[63] Nhan, T., et al., *Drug delivery to the brain by focused ultrasound induced blood–brain barrier disruption: Quantitative evaluation of enhanced permeability of cerebral vasculature using two-photon microscopy*. Journal of Controlled Release, 2013. **172**(1): p. 274-280.

[64] Lifshin, E., Y.P. Kandel, and R.L. Moore, *Improving Scanning Electron Microscope Resolution for Near Planar Samples Through the Use of Image Restoration*. Microscopy and Microanalysis, 2014. **20**(1): p. 78-89.

[65] Miranda, A., et al., *How did correlative atomic force microscopy and super-resolution microscopy evolve in the quest for unravelling enigmas in biology?* Nanoscale, 2021. **13**(4): p. 2082-99.

[66] Heinzelmann, H. and D.W. Pohl, *Scanning near-field optical microscopy*. Applied Physics A, 1994. **59**(2): p. 89-101.

[67] Bethe, H.A., *Theory of Diffraction by Small Holes*. Physical Review, 1944. **66**(7-8): p. 163-182.

[68] Ingham, J., et al., *An evaluation of the application of the aperture infrared SNOM technique to biomedical imaging*. Biomedical Physics & Engineering Express, 2018. **4**(2): p. 025011.

[69] Shershulin, V.A., et al., *Use of scanning near-field optical microscope with an aperture probe for detection of luminescent nanodiamonds*. Laser Physics, 2016. **27**(2): p. 025201.

[70] Betzig, E. and R.J. Chichester, *Single Molecules Observed by Near-Field Scanning Optical Microscopy*. Science, 1993. **262**(5138): p. 1422-1425.

[71] Mitrofanov, O., et al., *Photoconductive Terahertz Near-Field Detector with a Hybrid Nanoantenna Array Cavity*. ACS Photonics, 2015. **2**(12): p. 1763-1768.

[72] Wang, L. and X.G. Xu, *Scattering-type scanning near-field optical microscopy with reconstruction of vertical interaction*. Nature Communications, 2015. **6**(1): p. 8973.

[73] Huber, A.J., et al., *Terahertz Near-Field Nanoscopy of Mobile Carriers in Single Semiconductor Nanodevices*. Nano Letters, 2008. **8**(11): p. 3766-3770.

[74] Wei, B., et al. *Terahertz s-SNOM with > λ/1000 resolution based on self-mixing in quantum cascade lasers*. in 2017 European Conference on Lasers and Electro-Optics and European Quantum Electronics Conference. 2017. Munich: Optica Publishing Group.

[75] Wang, H., L. Wang, and X.G. Xu, *Scattering-type scanning near-field optical microscopy with low-repetition-rate pulsed light source through phase-domain sampling*. Nature Communications, 2016. **7**(1): p. 13212.

[76] Mason, D.R., M.V. Jouravlev, and K.S. Kim, *Enhanced resolution beyond the Abbe diffraction limit with wavelength-scale solid immersion lenses*. Optics Letters, 2010. **35**(12): p. 2007-2009.

[77] Zatta, R., et al., *Resolution Limits of Hyper-Hemispherical Silicon Lens-Integrated THz Cameras Employing Geometrical Multiframe Super-Resolution Imaging*. IEEE Transactions on Terahertz Science and Technology, 2021. **11**(3): p. 277-286.

[78] Yue, L., et al., *A Millimetre-Wave Cuboid Solid Immersion Lens with Intensity-Enhanced Amplitude Mask Apodization*. Journal of Infrared, Millimeter, and Terahertz Waves, 2018. **39**(6): p. 546-552.

[79] Lu, Y., et al., *Spherical aberration correction in aplanatic solid immersion lens imaging using a MEMS deformable mirror*. Microelectronics Reliability, 2012. **52**(9-10): p. 2120-2.

[80] Novitsky, A., et al., *Subwavelength Hyperlens Resolution With Perfect Contrast Function*. Annalen der Physik, 2018. **530**(3): p. 1700300.

[81] Darafsheh, A., et al., *Advantages of microsphere-assisted super-resolution imaging technique over solid immersion lens and confocal microscopies*. Applied Physics Letters, 2014. **104**(6).

[82] Wang, S., et al. *Terahertz dielectric properties of MgO-TiO2-ZnO based ceramics*. in 2015 40th International Conference on Infrared, Millimeter, and Terahertz waves (IRMMW-THz). 2015.

[83] Yu, C., et al. *High Permittivity and Low-Loss Millimeter-wave Dielectric Ceramics*. in 2018 11th UK-Europe-China Workshop on Millimeter Waves and Terahertz Technologies (UCMMT). 2018.

[84] Liu, Z., et al., *Polarization-independent metamaterial with broad ultrahigh refractive index in terahertz region*. Optical Materials Express, 2015. **5**(9): p. 1949-1953.

[85] Jiang, L., et al., *Terahertz high and near-zero refractive index metamaterials by double layer metal ring microstructure*. Optics & Laser Technology, 2020. 123: p. 105949.

[86] Pimenov, A. and A. Loidl, *Focusing of millimeter-wave radiation beyond the Abbe barrier*. Applied Physics Letters, 2003. **83**(20): p. 4122-4124.

[87] Ippolito, S.B., et al., *High spatial resolution subsurface thermal emission microscopy*. Applied Physics Letters, 2004. **84**(22): p. 4529-4531.

[88] Fletcher, D.A., et al., *Refraction contrast imaging with a scanning microlens*. Applied Physics Letters, 2001. **78**(23): p. 3589-3591.

[89] Gompf, B., et al., *THz-micro-spectroscopy with backward-wave oscillators*. Infrared Physics & Technology, 2006. **49**(1): p. 128-132.

[90] Köklü, F.H., et al., *Widefield subsurface microscopy of integrated circuits*. Optics Express, 2008. **16**(13): p. 9501-9506.

[91] Jin, Y.-S., G.-J. Kim, and S.-G. Jeon, *Terahertz dielectric properties of polymers*. Journal of the Korean Physical Society, 2006. **49**(2): p. 513-517.

[92] Giannacopoulos, S., *Étude sur les composites céramiques-polymères pour l'imagerie THz par immersion solide*, in Final report for the Maîtrise Cours under the supervision of Prof. M. Skorobogatiy. 2019, Polytechnique: Montreal.

[93] Ung, B., et al., *High-refractive-index composite materials for terahertz waveguides: trade-off between index contrast and absorption loss*. Journal of the Optical Society of America B, 2011. **28**(4): p. 917-921.

[94] Porzucek, K., *Deduction of the temperature dependence of the stiffness from softening temperature measurements*. Polymer Testing, 1992. **11**(1): p. 23-35.

[95] Yan, M.F. and W.W. Rhodes, *Low temperature sintering of TiO2*. Materials Science and Engineering, 1983. **61**(1): p. 59-66.

[96] Chao, S., V. Petrovsky, and F. Dogan, *Effects of sintering temperature on the microstructure and dielectric properties of titanium dioxide ceramics*. Journal of Materials Science, 2010. **45**(24): p. 6685-6693.

[97] Liao, S.-C., K.D. Pae, and W.E. Mayo, *High pressure and low temperature sintering of bulk nanocrystalline TiO2*. Materials Science and Engineering: A, 1995. **204**(1): p. 152-159.

[98] Vaidya, N. and O. Solgaard, *3D printed optics with nanometer scale surface roughness*. Microsystems & Nanoengineering, 2018. **4**(1): p. 18.

[99] Tan, W.S., et al., *3D printing by selective laser sintering of polypropylene feed channel spacers for spiral wound membrane modules for the water industry*. Virtual and Physical Prototyping, 2016. **11**(3): p. 151-158.

[100] Wu, J., *Study on optimization of 3D printing parameters*. IOP Conference Series: Materials Science and Engineering, 2018. 392: p. 062050.

[101] Wang, L. and D.J. Gardner, *Effect of fused layer modeling (FLM) processing parameters on impact strength of cellular polypropylene*. Polymer, 2017. 113: p. 74-80.

[102] Salmon, A., et al., *Rapid prototyping of flexible terahertz metasurfaces using a microplotter*. Optics Express, 2021. **29**(6): p. 8617-8625.

[103] Spoerk, M., et al., *Polypropylene Filled With Glass Spheres in Extrusion-Based Additive Manufacturing: Effect of Filler Size and Printing Chamber Temperature*. Macromolecular Materials and Engineering, 2018. **303**(7): p. 1800179.

[104] Olam, M. and N. Tosun, *Assessment of 3D Printings Produced in Fused Deposition Modeling Printer Using Polylactic Acid/TiO2/Hydroxyapatite Composite Filaments*. Journal of Materials Engineering and Performance, 2022.

[105] Danks, A.E., S.R. Hall, and Z. Schnepp, *The evolution of 'sol–gel' chemistry as a technique for materials synthesis*. Materials Horizons, 2016. **3**(2): p. 91-112.

[106] Ivanova, T., et al. *Electrochromic and optical study of sol-gel TiO2-MnO films*. in 21st International Summer School on Vacuum, Electron and Ion Technologies, 23-27 Sept. 2019. 2020. UK: IOP Publishing.

[107] Yu, W.X. and X.C. Yuan, *Fabrication of refractive microlens in hybrid SiO2/TiO2 sol-gel glass by electron beam lithography*. Optics Express, 2003. **11**(8): p. 899-903.

[108] Messaddeq, S.H., et al., *Photopolymerized hybrids containing TiO2 nanoparticles for gradient-index lens*. Materials Chemistry and Physics, 2019. 236: p. 121793.

[109] Miao, L., et al., *Simultaneous epitaxial growth of anatase and rutile TiO2 thin films by RF helicon magnetron sputtering*. Journal of Crystal Growth, 2003. **254**(1): p. 100-106.

[110] Lin, Z.A., et al., *Facile fabrication and tuning of TiO2 nanoarchitectured morphology using magnetron sputtering and its applications to photocatalysis*. Ceramics International, 2014. **40**(10): p. 15523-15529.

[111] Cheng, F., et al., *Porous single-crystalline titanium dioxide at 2 cm scale delivering enhanced photoelectrochemical performance*. Nature Communications, 2019. **10**(1): p. 3618.

[112] Mitrofanov, O., et al., *Magnetic dipole and electric dipole resonances in TiO2 microspheres at terahertz frequencies*. SPIE OPTO. Vol. 9370. 2015: SPIE.

[113] Skocaj, M., et al., *Titanium dioxide in our everyday life; is it safe?* Radiol Oncol, 2011. **45**(4): p. 227-47.

[114] Nallappan, K., et al., *Dispersion-limited versus power-limited terahertz communication links using solid core subwavelength dielectric fibers*. Photonics Research, 2020. **8**(11): p. 1757-1775.

[115] Chernomyrdin, N., et al., *Terahertz transmission-mode near-field scanning-probe microscope based on a flexible sapphire fiber*. SPIE Nanoscience + Engineering. Vol. 11088. 2019: SPIE.

[116] Richards, D., et al., *Near-field microscopy by elastic light scattering from a tip*. Philosophical Transactions of the Royal Society of London. Series A: Mathematical, Physical and Engineering Sciences, 2004. **362**(1817): p. 787-805.

[117] Kino, G.S. *Solid immersion lens*. in Optical Engineering for Sensing and Nanotechnology (ICOSN'99). 1999. International Society for Optics and Photonics.

[118] Kino, G.S. *Applications and theory of the solid immersion lens. in Optical Pulse and Beam Propagation*. 1999. International Society for Optics and Photonics.

[119] Suzuki, T., K. Endo, and S. Kondoh, *Terahertz metasurface ultra-thin collimator for power enhancement*. Optics Express, 2020. **28**(15): p. 22165-22178.

[120] Jing, X., et al., *Design of ultrahigh refractive index metamaterials in the terahertz regime*. Superlattices and Microstructures, 2017. 109: p. 716-724.

[121] Fan, W., et al., *Three-dimensional all-dielectric metamaterial solid immersion lens for subwavelength imaging at visible frequencies*. Science Advances, 2016. **2**(8).

[122] Kocic, N., et al., *Lenses for terahertz applications: Development of new materials and production processes*. AIP Conference Proceedings, 2014. **1593**(1): p. 416-419.

[123] Buesser, B., A.J. Gröhn, and S.E. Pratsinis, *Sintering Rate and Mechanism of TiO2 Nanoparticles by Molecular Dynamics*. The Journal of Physical Chemistry C, 2011. **115**(22): p. 11030-11035.

[124] Liao, S.-C., K.D. Pae, and W.E. Mayo, *High pressure and low temperature sintering of bulk nanocrystalline TiO2*. Materials Science and Engineering: A, 1995. **204**(1): p. 152-159.

[125] Barringer, E.A. and H.K. Bowen, *Formation, Packing, and Sintering of Monodisperse TiO2 Powders*. Journal of the American Ceramic Society, 1982. **65**(12): p. C-199-C-201.

[126] Guerboukha, H., et al., *Planar Porous Components for Low-Loss Terahertz Optics*. Advanced Optical Materials, 2019. **7**(15): p. 1900236.

[127] Rane, A.V., et al., *Chapter 5 - Methods for Synthesis of Nanoparticles and Fabrication of Nanocomposites, in Synthesis of Inorganic Nanomaterials*, S. Mohan Bhagyaraj, et al., Editors. 2018, Woodhead Publishing. p. 121-139.

[128] Wang, X., et al., *High refractive index composite for broadband antireflection in terahertz frequency range*. Applied Physics Letters, 2015. **106**(23): p. 231107.

[129] Cao, M., et al., *Multiparameter optimization design of chemical mechanical polishing for planar optics*. The International Journal of Advanced Manufacturing Technology, 2021. **113**(7): p. 2153-2162.

[130] Roggenbuck, A., et al., *Using a fiber stretcher as a fast phase modulator in a continuous wave terahertz spectrometer*. Journal of the Optical Society of America B: Optical Physics, 2012. **29**(4): p. 614-620.

[131] Matsumoto, N., et al., *Analysis of Dielectric Response of TiO2in Terahertz Frequency Region by General Harmonic Oscillator Model*. Japanese Journal of Applied Physics, 2008. **47**(9): p. 7725-7728.